

Hydrogen bonding in water under extreme confinement unveiled by nanoscale vibrational spectroscopy and simulations

Xintong Xu^{†1}, Xin Jin^{†2,3}, Matthias Kuehne⁴, De-Liang Bao², Joel Martis¹, Yu-Ming Tu⁴, Cody L. Ritt⁴, Juan Carlos Idrobo⁵, Michael S. Strano⁴, Arun Majumdar^{*1,6,7}, Sokrates T. Pantelides^{*2,8}, Jordan A. Hachtel^{*9}

[†]Equally Contributing First Authors

¹Department of Mechanical Engineering, Stanford University, Stanford, CA, USA

²Department of Physics and Astronomy, Vanderbilt University, Nashville, TN, USA

³University of the Chinese Academy of Sciences, Beijing 100049, China

⁴Department of Chemical Engineering, Massachusetts Institute of Technology, MA, USA

⁵Materials Science & Engineering, University of Washington, Seattle, WA, USA

⁶Precourt Institute for Energy, Stanford University, Stanford, CA, USA

⁷Department of Photon Science, SLAC National Laboratory, Menlo Park, CA, USA

⁸Department of Electrical and Computer Engineering, Vanderbilt University, Nashville, TN, USA

⁹Center for Nanophase Materials Sciences, Oak Ridge National Laboratory, Oak Ridge, TN, USA

*Correspondence to: arunava@stanford.edu

*Correspondence to: pantelides@vanderbilt.edu

*Correspondence to: hachtelja@ornl.gov

Notice: This manuscript has been authored by UT-Battelle, LLC, under Contract No. DE-AC0500OR22725 with the U.S. Department of Energy. The United States Government retains and the publisher, by accepting the article for publication, acknowledges that the United States Government retains a non-exclusive, paid-up, irrevocable, world-wide license to publish or reproduce the published form of this manuscript, or allow others to do so, for the United States Government purposes. The Department of Energy will provide public access to these results of federally sponsored research in accordance with the DOE Public Access Plan (<http://energy.gov/downloads/doe-public-access-plan>).

Fluids under extreme confinement exhibit distinctly new properties compared to their bulk analogs¹⁻⁵. Understanding the structure and intermolecular bonding of confined water lays the foundation for creating and improving applications at the water-energy nexus⁶⁻⁸. However, probing confined water experimentally at the length scale of intermolecular and surface forces has remained a challenge. Here, we report a combined experiment/theory framework to reveal changes in H-bonding environment and the underlying molecular structure of confined water inside individual carbon nanotubes. H-bonding is directly probed through the O-H stretch frequency with vibrational electron energy-loss spectroscopy and compared to spectra from molecular-dynamics simulations based on density-functional-theory. Experimental spectra show that water in larger carbon nanotubes exhibit the bonded O-H vibrations of bulk water, but at smaller diameters, the frequency blueshifts to near the ‘free’ O-H stretch found in water vapor and hydrophobic surfaces. The matching simulations reveal that, in addition to steric confinement, the tube’s vibrations play a key role in breaking up the H-bond network, resulting in an orientationally-dispersed, non-H-bonded phase. Furthermore, the temperature-dependence of the vibrations is investigated, providing insights into phase transitions and the confined-water density. This

research demonstrates the potential of the experiment/theory framework to explore unprecedented aspects of structure and bonding in confined fluids.

Introduction

Exotic behaviors in fluids emerge when they are under extreme confinement in nanoscale channels, cavities and porous media, whose length scales match the fundamental range of intermolecular and surface forces. Carbon nanotubes (CNTs) with atomically smooth inner surfaces and diameters in the range of 1-2 nm, resemble biological water channels, and give rise to significant enhancement of water transport, orders of magnitude faster than that in bulk¹⁻⁵. The anomalous behaviors rely on the structure of water confined water, which can be characterized by the hydrogen-bond (H-bond) network - a subtle interplay of localized bonding and long-range interactions, where the varied H-bond networks give rise to diverse phases of water layers at surfaces and interfaces⁹⁻¹¹. Deeper understanding of the complex structure of water in CNTs and the interactions of confined fluids with their bounding surfaces would facilitate new technologies at the water-energy nexus⁶⁻⁸.

Experimental examinations of the structure of water in CNTs has mostly been conducted with macroscopic optical and beam-line techniques on ensembles of CNTs with non-uniform diameters¹²⁻¹⁸. Even in experiments that leverage sparsity to isolate CNTs from one another¹⁹, the limited cross-section of the macroscopic beam with a single tube prevents direct analysis of water within. Transmission electron microscopy has been used to examine individual CNTs at high spatial resolution²⁰. However, given the mobile nature of liquid water and light atomic weight of H, directly imaging the H-bond network using electron microscopy is a major challenge.

As a result, molecular-dynamics (MD) simulations have been the primary method to access the atomic-scale structure and H-bond network information of water inside individual CNTs. The predicted structures demonstrate a strong dependence on the inner diameter; ranging from bulk-like water in large-diameter CNTs ($d > 2$ nm) to ordered ‘ice-tubes’ or disordered tubular structures in medium-diameter CNTs ($d \sim 1-2$ nm) to one-dimensional chains in small-diameter CNTs ($d < 1$ nm)^{12,15,21-30}. Both classical²¹ and density functional theory (DFT)-based²⁶ MD found that, in medium-diameter CNTs, water features vibrational modes at ~ 420 meV (‘bonded’ O-H stretch as in bulk water) and ~ 460 meV (‘free’ O-H stretch as found in water vapor³¹ and at hydrophobic interfaces⁹), where the primary difference between the two stretch modes is whether the H atom is bonded to a neighboring water molecule’s O atom. Early MD simulations in 2000, based on classical potentials³², led to the conclusion that the confinement drove the structural changes and that the CNT vibrations have minimal effects, leading to a large fraction of subsequent simulations employing rigid CNTs. While flexible CNTs have been more utilized in recent years, the focus on CNT vibrations has mainly been on their influence on transport^{27,33-35}. Possible effects of CNT vibrations on the confined-water H-bond network have not been addressed. Furthermore, the above

theoretical results have not been validated by experiments which can access the water vibrations of individual CNTs.

A spectroscopic option that matches the length scale of individual CNTs is vibrational electron energy-loss spectroscopy (vEELS) in the monochromated scanning transmission electron microscope (STEM). vEELS can currently attain energy resolution in the range of 3-4 meV ($25\text{-}30\text{ cm}^{-1}$)³⁶, while maintaining sub-nanometer spatial resolution³⁷, which allows us to directly measure molecular vibrations³⁸⁻⁴¹, including the O-H stretch of water⁴². Since *intermolecular* H \cdots O bonds mediate the vibrational frequency of the *intramolecular* O-H stretch¹⁰, the O-H stretch frequency is a natural probe of the H-bonding environment. Here, we combine vEELS with DFT-MD simulations to unveil the H-bonding and molecular structure of confined water. Our results show that the vibrational response is highly dependent on the diameter of CNTs, the vibrations of the CNT wall, the density of the water inside the tube, and the temperature of the system.

Visualizing Water in Individual CNTs with vEELS

A schematic of the vEELS experiments is shown in Fig. 1a. The CNTs are directly grown on SiN_x TEM grids with arrays of 200 nm holes by chemical vapor deposition (CVD). Afterwards, grown tubes are cut open by focused ion beam and placed in a humidifier to allow water infiltration (Supplementary Fig. S1). The CNTs are sparse, millimeters long, and cross the membrane in parallel, making them easy to identify and isolate, as shown in Fig. 1b. STEM reference images are acquired with a high-angle annular dark-field (HAADF) detector, shown in Fig. 1c, enabling

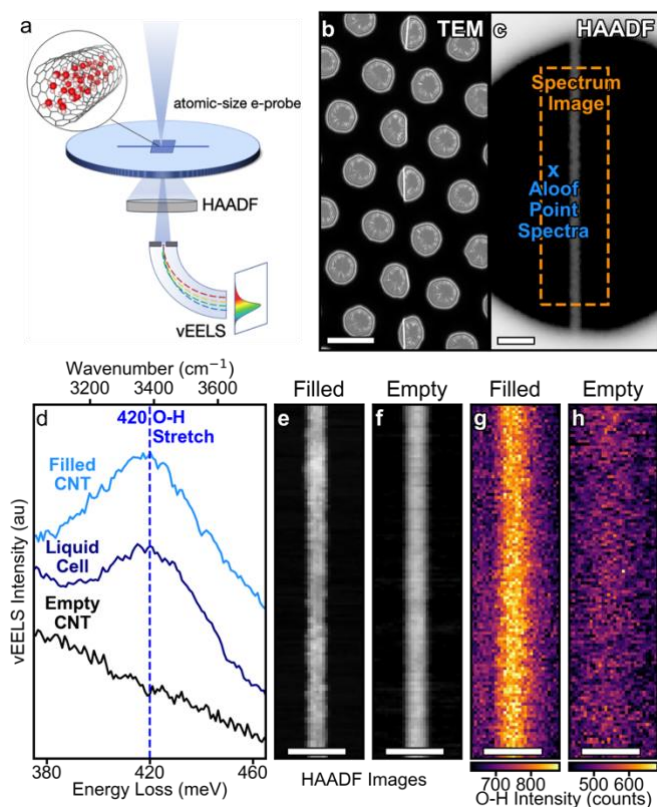


Fig. 1. Visualization of water confined in a single carbon nanotube. (a) Schematic of the vibrational electron energy-loss spectroscopy (vEELS) experimental setup. (b) Low-magnification TEM image of nanotubes on 200 nm diameter holey SiN grid. Scale bar is 500 nm. (c) HAADF image of a CNT. Annotations denote representative probe position for aloof point spectra acquisitions, and the scanned region for a spectrum. Scale bar – 50 nm. (d) Aloof vEEL spectra of a filled CNT (top), a bulk-water liquid cell (middle) and an empty CNT (bottom); the filled tube features a single peak at 420 meV that matches the peak of the bulk-water vEEL spectrum. (e-h) vEEL spectrum images of filled and empty tubes from (d). Scale bars – 20 nm. (e,f) HAADF images of filled (e) and empty (f) CNTs. (g,h) Spectrum image slices integrating the intensity of the O-H stretch vibrations (between 400 and 500 meV) for the filled (g) and empty (h) tubes, showing the clear spatial signature of water confined inside the tube.

precision control of the beam for vEELS acquisitions. To minimize beam damage, we primarily acquire ‘aloof’ point spectra, where the beam is placed closed to the sample (~ 30 nm), without directly intersecting it, and the vibrations are probed through the evanescent interactions⁴³. We also acquire spectrum images, where EEL spectra are acquired at each probe position in a 2D grid to create a full hyperspectral dataset, which enables the localization of the vibrations to be directly measured.

Figure 1d shows vEEL spectra from two different nominally water-filled CNTs compared with vEELS recorded from a bulk liquid cell. One CNT (bottom) appears empty, with no peak in the O-H stretch regime. However, the other CNT (top) shows a dominant peak at 420 meV, consistent in both linewidth and frequency to the bulk-water O-H stretch obtained from a liquid cell. The match verifies the existence of water in the CNT and demonstrates the capacity of vEELS to directly interrogate water vibrations in a confined CNT environment. Spectrum images are also acquired from the CNTs from Fig. 1d. The HAADF images are shown in Fig. 1e (filled) and Fig. 1f (empty) exhibiting no clear differences. By integrating the spectrum in each pixel between 400 and 500 meV (the O-H stretch regime), we can see in Fig. 1g that the filled tube lights up, while Fig. 1h shows that the empty tube has barely any variation from the background.

The Effect of Confinement and CNT Vibrations on H-Bonding

To explore the H-bonding of water under extreme confinement, we probed the frequency of O-H stretch modes in water-filled CNTs with different diameters. Figure 2a compares the room temperature (RT) vibrational spectra of water within CNTs with inner diameters (d) of 2.3 and 1.4 nm. TEM images of the tubes used to measure the inner diameters are shown in the Supplementary Fig. S2. The 2.3-nm-diameter CNT spectrum matches with the spectrum of bulk water, *i.e.*, a single vibrational peak at 420 meV (3400 cm^{-1}), while in the more confined system, namely the 1.4-nm-diameter CNT, the vibrational peak blueshifts to ~ 455 meV ($\sim 3700\text{ cm}^{-1}$). This is the frequency of the free O-H stretch which is observed in vapor and hydrophobic surfaces/interfaces^{9,31}. The domination of the vibrational response by the free O-H stretch shows that the water molecules are weakly or non-H-bonded, indicating the emergence of an unusual phase of confined water with an almost total disruption of the H-bond network.

The origin of this change in H-bonding can be revealed by comparisons with the vibrational densities of states (vDOS) generated by DFT-MD simulations. In Fig. 2b, we compare the vDOS of bulk water to that of water-filled-CNTs simulated under two conditions: one where the CNT wall is held rigid and one where the wall is free to vibrate during the MD run. To reduce computation costs, accurate DFT-MD simulations were performed for CNTs with a diameter of 1.1 nm. Select simulations for diameters of 1.4 nm verify that the results are essentially identical, as shown in Supplemental Fig. S3, indicating that the 1.1 nm diameter simulations are representative of the medium-diameter range, $d=1.1-1.4$ nm.

The computationally predicted bulk water vDOS (Fig. 2b top) is in excellent agreement with the experimental vEELS of bulk water and the 2.3 nm CNT. The vDOS of the rigid CNT displays a sharp high-frequency peak at ~ 460 meV while retaining a broad peak at 420 meV (Fig. 2b middle), corresponding to free and bonded O-H respectively. This result is consistent with previous reports^{21,26}, which found that the steric constraints of a rigid hydrophobic CNT produce a partial breakdown of the H-bond network that causes the emergence of the free O-H stretch. On the other hand, when the vibrations of the CNT walls are included, the vDOS exhibits a single broad peak at ~ 455 meV (Fig 2b bottom) in full accord with the experimental vEELS. We note that the vEELS energy-resolution (~ 8.5 meV) is demonstrably sufficient to distinguish between the two spectra shown in Fig. 2b (Supplemental Fig. S4).

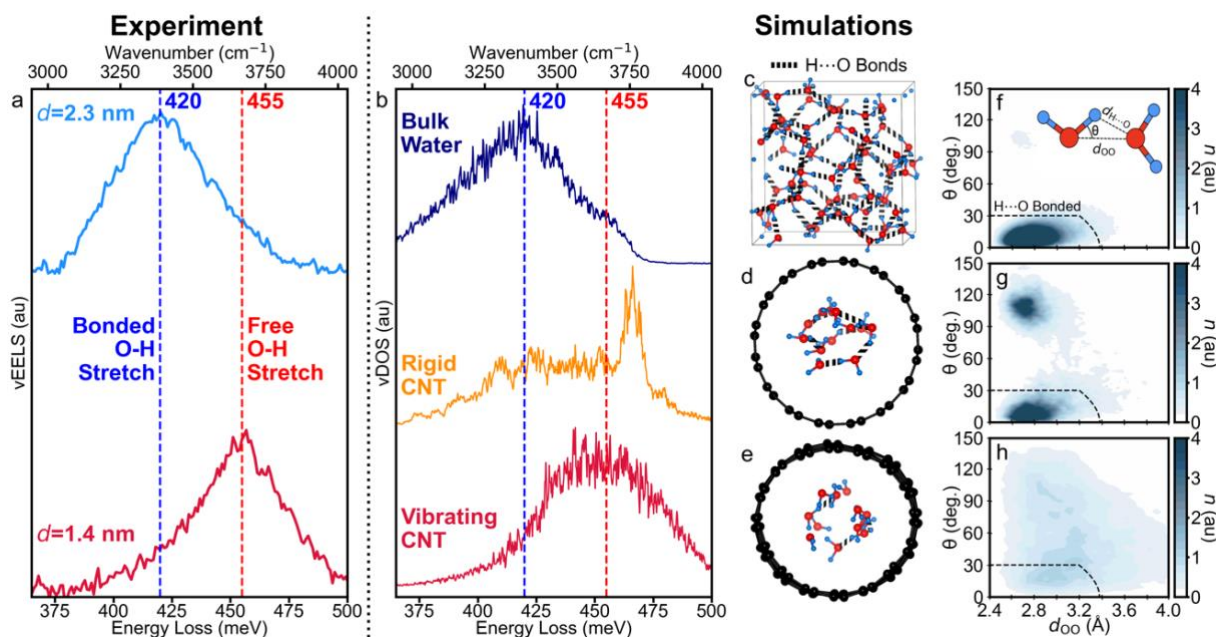


Figure 2. Vibrational properties and hydrogen bonding of water confined in medium diameter CNTs. (a) vEEL spectra from tubes with different inner diameters: 2.3 nm – top (same as Fig. 1) and 1.4 nm – bottom. The larger tube exhibits the ‘bonded’ O-H stretch, i.e., the O-H \cdots O stretch at 420 meV (3400 cm^{-1}) while the smaller tube exhibits ‘free’ O-H stretch frequency 455 meV (3670 cm^{-1}). (b) Calculated vibrational densities of states (vDOS): bulk water (top), water in a rigid-walled tube CNT (middle), and water in a vibrating-walled CNT (bottom). Both simulated CNTs have an inner diameter of 1.1 nm which is representative of medium diameter CNTs, $d=1.1$ -1.4 nm. (c-e) DFT-MD snapshots for the bulk water (c), rigid CNT (d) and vibrating CNT (e) in (b). Here, the intermolecular H \cdots O bonds are highlighted with black dotted lines, showing that the vibrating tube results in near-total elimination of H \cdots O bonds. (f-g) d_{OO} vs. θ heatmaps corresponding to the relative distances and orientations of water molecules throughout the simulations. Dashed line indicates region where H \cdots O bonding occurs, corresponding to $\theta < 30^\circ$ and $d_{\text{H}\cdots\text{O}} < 2.4 \text{ \AA}$. The quantities d_{OO} and θ are defined as the nearest neighbor O distances and H-bond angles, as indicated in the schematic in the inset of (f). All experiments and simulations at 300 K.

The molecular structure that corresponds to the vDOS of the vibrating CNT can now be extracted from the atomic positions in the MD simulations, highlighted in Figs. 2c-h. Representative snapshots of the MD simulations for vDOS in Fig. 2b are shown for bulk water, a rigid CNT, and a vibrating CNT in Figs. 2c-e, respectively. Here, intermolecular H \cdots O bonds are marked with

dark dotted lines when the H \cdots O distance is less than 2.4 Å and the bond angle (as defined on the inset in Fig. 2f) is less than 30°³². In the rigid CNT snapshot, Fig. 2d, we can see that, while the H-bond network is less ubiquitous compared to bulk water (Fig 2c), a large fraction of the molecules are still H-bonded and many of the non-H-bonded molecules are oriented towards the CNT wall. However, in the vibrating CNT snapshot, Fig. 2e, there are hardly any H \cdots O bonds, indicating a near-total disruption of the H-bond network.

For better visualization, statistical heatmaps of the hydrogen bonding throughout the course of each MD simulation are shown in Fig. 2f-h, for bulk water, the rigid CNT, and the vibrating CNT respectively. To generate the heatmap, in every snapshot of the MD simulations, we identify the first (intramolecular) and second (intermolecular) O neighbor of every H atom and measure this OO distance (d_{oo}) and the tilt angle of the H atom to this line (see the inset in Fig. 2f). The heatmap of bulk water has an average d_{oo} of 2.7 ± 0.3 Å and θ of $10^\circ\pm 5^\circ$. The heatmap of the rigid CNT shows a bimodal distribution, with a mixture of molecules with O-H in the bonded configuration, as in bulk water, and a group with O-H in a fundamentally different orientation, where d_{oo} is still less than 3 Å but now the bond angles are also between 90° and 120°. These orientations are consistent with molecules oriented towards the CNT wall, as seen in the rigid-CNT snapshot in Fig. 2d. In the heatmap of the vibrating CNT, on the other hand, the statistical distributions in d_{oo} and θ are broad, extending well past 3 Å and populating all angles between 0° and 120°, *i.e.*, the molecular orientations are relatively evenly and randomly spread throughout the angle/distance parameter space. The agreement between the experimental vEELS and simulated vDOS for the vibrating CNT suggests that the single broad peak observed at ~455 meV, along with the disruptions in the H-bond network observed in the MD simulations, correspond to an unusual new phase of water we term ‘non-H-bonded water’. Furthermore, the lack of agreement between the experimental vEELS and simulated vDOS for the rigid CNT demonstrates that the vibrations of the tube are critical to achieving this non-H-bonded phase. The vibrations further equalize the energy between water molecules and breaks the H bond network through water-wall interactions.

MD simulations were performed for water densities ranging from $\rho = 0.5$ to 1.5 g/cm³. They show that the non-H-bonded phase occurs for all densities if the CNT carbon atoms are allowed to vibrate, while the bimodal bonding phase occurs for all densities if the CNT is held rigid. Extensive tests using best-of-breed DFT functionals further confirmed the robustness of the results (see Methods). The complete results for vDOS, MD snapshots, and heatmaps for all densities and functionals, and both rigid and vibrating CNTs are shown in Supplementary Figs. S5-S12. While all densities produce similar results at 300 K significant variations are observed between densities at 100 K, which will be expanded upon in the following section. The vDOS in the above figure (Fig. 2b-h) shows representative results for $\rho = 0.5$ g/cm³, which we will show exhibits the best spectral match to vEELS on the 1.4 nm diameter CNT at 100 K in the following section.

Temperature-Dependent Response of Confined Fluids

For water under extreme confinement, subtle changes in the competition between molecule-wall and molecule-molecule interactions can fundamentally change the phase diagram since they are of comparable strengths in these systems. This competition opens many possibilities of variations in the H-bond network and of numerous phases of water and ice⁴⁴. Here we report initial vEELS at 100 K for the 1.4-nm-diameter and 2.3-nm-diameter CNTs that we studied at room temperature (Fig. 2) and select MD simulations that apply to these cases.

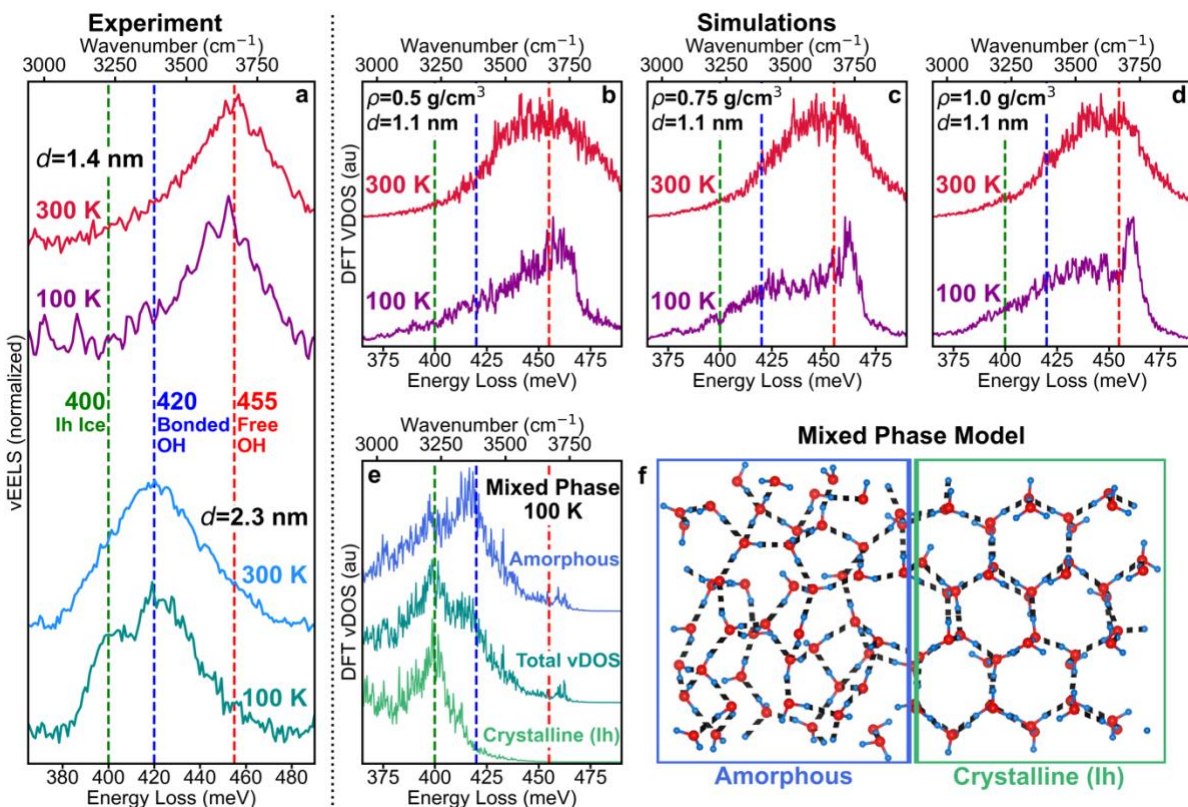


Fig. 3. Vibrational response at cryogenic and room temperature in filled CNTs. (a) vEEL spectra at 300 K and 100 K for the 1.4-nm-diameter CNT (top) and 2.3-nm-diameter CNT (bottom). (b-d) Calculated vibrational densities of states (vDOS) at 300 K (top) and 100 K (bottom) for medium diameter CNTs ($d=1.1$ nm) with water densities of $\rho=0.5$ g/cm³ (b), 0.75 g/cm³ (c), and 1.0 g/cm³ (d), demonstrating the evolution of the vibrational spectrum of water in medium-diameter tubes as a function of water density. (e,f) vDOS for a mixed ice model composed of amorphous and crystalline regions. vDOS for amorphous region (top), total supercell (center), and crystalline region (bottom) in (e), supercell used for calculation with amorphous and crystalline regions marked in (f).

The vEEL spectra were taken by lowering the temperature from 300 K to 100 K with a cryogenic STEM holder. The vEEL spectra are plotted in Fig. 3a. They show that the 1.4-nm-diameter CNT undergoes no significant change in peak frequency or lineshape, while the 2.3-nm-diameter CNT exhibits a secondary peak at 400 meV that emerges only at cryogenic temperatures. The change also appears to be reversible, as the vEEL spectrum acquired upon returning to room temperature does not exhibit the 400 meV peak (shown in Supplementary Figure S13). These observations

indicate that, for the smaller-diameter CNT, the non-H-bonded water phase from the RT measurements in Fig. 2 appears to persist to 100 K, while for the higher diameter CNT, water undergoes a partial phase transition. Similar effects have been observed in nano-droplets and mesoporous membranes, and the Raman spectra of filled CNTs, where reformation of the H-bond network is suppressed when lowering temperature for small droplet diameters and pore sizes^{19,45,46}.

For the smaller-diameter CNT, we performed MD simulations for several water densities, since it impacts the ratio of molecule-wall and molecule-molecule interactions and hence influence the temperature-dependence of the system. The vDOS for the 1.1-nm-diameter CNT is shown for three different water densities (0.5, 0.75, and 1.0 g/cm³) at both 300 K and 100 K in Figs 3b-d. As already mentioned at the end of the previous section, at 300 K, the vDOS for all three water densities are qualitatively quite similar, but at 100 K, the vDOS of the two higher water densities transform from the non-H-bonded water phase to the bimodal line-shape of water in rigid CNTs (see Supplementary Fig. S5). The MD snapshots and heatmaps for these densities at 100 K also exhibit a strong match to the 300 K rigid CNT simulations (see Supplementary Figs. S6-S7), indicating that structure strongly matches the mixed-bonding water phase. Conversely, for the lowest water density (0.5 g/cm³) at 100 K, the confined water remains in the non-H-bonded phase, resulting in a single-peak vDOS that agrees with the vEELS in Fig. 3a. The MD simulations demonstrate that the density-dependent evolution of the vibrational response reveals itself at cryogenic temperatures, which, in conjunction with vEELS, can potentially be a mechanism to measure density in confined fluids (see Supplementary Fig. S14).

For the 2.3-nm-diameter CNT, we note that the emergent peak at 400 meV is consistent with the Ih phase of ice with tetrahedrally-coordinated molecules¹² and that vEELS experiments on bulk amorphous ice have shown vibrations at 420 meV⁴⁷. A combination of different phases of ice would naturally lead to the combined peaks at 400 and 420 meV as we observed here in vEELS. Moreover, previous predictions have indicated that different phases of ice with different average H-bond numbers can exist simultaneously inside layered nanotube-ice⁴⁸. To visualize this effect, the vDOS at 100 K of a mixed ice supercell is calculated and shown in Fig. 3e, with the schematic of the supercell in Fig. 3f. The projected vDOS from the amorphous region (top) exhibits a broad peak with its maximum intensity at 420 meV while the crystalline region (bottom) exhibits a sharp peak at 400 meV. As a result, the total vDOS (center) features both peaks, albeit with a different ratio of intensities on the two peaks, demonstrating that the experiment is consistent with a transition to a phase of ice with a mixed and complex H-bond network.

We note that in a repeat experiment, we observed a qualitatively similar, but far less pronounced, phase change signature in a 4.2 nm-diameter CNT. The repeat experiment as well as additional discussion on the advantages and limitations of the present analysis are included in Supplementary Discussion 2.

Our results reveal how the H-bonding and structures of confined water change with the unexpected effects of CNT wall vibrations, along with the size-, temperature- and density-dependence, as they synergistically alter the competition of molecule-molecule and molecule-wall interactions. The powerful combination of high-energy/spatial-resolution vEELS experiments with cryo capabilities and DFT-MD simulations can reveal the likely organization as well as intermolecular and surface interactions of confined liquids, thus offering the promising prospects of new scientific advances in multiple disciplines.

Acknowledgments

This research was supported as part of the Center for Enhanced Nanofluidic Transport (CENT), an Energy Frontier Research Center funded by the U.S. Department of Energy (DOE), Office of Science, Basic Energy Sciences (BES), under Award # DE-SC0019112. Vibrational EELS research was supported by the Center for Nanophase Materials Sciences, (CNMS), which is a DOE Office of Science User Facility using instrumentation within ORNL's Materials Characterization Core provided by UT-Battelle, LLC, under Contract No. DE-AC05-00OR22725 with the DOE and sponsored by the Laboratory Directed Research and Development Program of Oak Ridge National Laboratory, managed by UT-Battelle, LLC, for the U.S. Department of Energy. Theoretical work at Vanderbilt University (X. J., D.-L. B., S. T. P.) was supported by the U.S. Department of Energy Office of Science, Basic Energy Sciences, Materials Science and Engineering Directorate Grant No. DE-FG02-09ER46554 and by the McMinn Endowment. X. J. is partially supported by the Fundamental Research Funds for the Central Universities. Computations were carried out in part at the National Energy Research Scientific Computer Center (NERSC), a U.S. Department of Energy Office of Science User Facility located at Lawrence Berkeley National Laboratory, operated under contract no. DE-AC02-05CH11231 and in part at the Beijing Three Axis Space Technology Co. Ltd. This work was led equally by Stanford University, Vanderbilt University and Oak Ridge National Laboratory.

Author Contributions

Experiments were conceived of and designed by XX, JCI, AM, and JAH. VEELS data was acquired and analyzed by XX and JAH with guidance from JM and AM. DFT calculations were conducted by XJ with guidance from DLB and STP. Samples were synthesized and prepared by XX, MK, YMT, CLR, and MSS. Manuscript and supplementary materials were written by XX, XJ, STP, and JAH. All authors contributed to the editing and revision of the manuscript.

Competing Interests Statement

The authors declare no competing interests.

Supplementary Information

Supplementary Information is available for this paper.

Correspondence

Correspondence and requests for materials should be addressed to arunava@stanford.edu, pantelides@vanderbilt.edu, or hachtelja@ornl.gov.

References

1. Hummer, G., Rasaiah, J. C. & Noworyta, J. P. Water conduction through the hydrophobic channel of a carbon nanotube. *Nature* **414**, 188–190 (2001).
2. Majumder, M., Chopra, N., Andrews, R. & Hinds, B. J. Enhanced flow in carbon nanotubes. *Nature* **438**, 44–44 (2005).
3. Holt, J. K. *et al.* Fast Mass Transport Through Sub-2-Nanometer Carbon Nanotubes. *Science* **312**, 1034–1037 (2006).
4. Secchi, E. *et al.* Massive radius-dependent flow slippage in carbon nanotubes. *Nature* **537**, 210–213 (2016).
5. Tunuguntla, R. H. *et al.* Enhanced water permeability and tunable ion selectivity in subnanometer carbon nanotube porins. *Science* **357**, 792–796 (2017).
6. Faucher, S. *et al.* Critical Knowledge Gaps in Mass Transport through Single-Digit Nanopores: A Review and Perspective. *J. Phys. Chem. C* **123**, 21309–21326 (2019).
7. Bocquet, L. Nanofluidics coming of age. *Nat. Mater.* **19**, 254–256 (2020).
8. Aluru, N. R. *et al.* Fluids and Electrolytes under Confinement in Single-Digit Nanopores. *Chem. Rev.* **123**, 2737–2831 (2023).
9. Scatena, L. F., Brown, M. G. & Richmond, G. L. Water at Hydrophobic Surfaces: Weak Hydrogen Bonding and Strong Orientation Effects. *Science* **292**, 908–912 (2001).
10. Montenegro, A. *et al.* Asymmetric response of interfacial water to applied electric fields. *Nature* **594**, 62–65 (2021).
11. Kapil, V. *et al.* The first-principles phase diagram of monolayer nanoconfined water. *Nature* **609**, 512–516 (2022).
12. Kolesnikov, A. I. *et al.* Anomalously Soft Dynamics of Water in a Nanotube: A Revelation of Nanoscale Confinement. *Phys. Rev. Lett.* **93**, 035503 (2004).
13. Maniwa, Y. *et al.* Ordered water inside carbon nanotubes: formation of pentagonal to octagonal ice-nanotubes. *Chemical Physics Letters* **401**, 534–538 (2005).
14. Matsuda, K., Hibi, T., Kadowaki, H., Kataura, H. & Maniwa, Y. Water dynamics inside single-wall carbon nanotubes: NMR observations. *Phys. Rev. B* **74**, 073415 (2006).
15. Byl, O. *et al.* Unusual Hydrogen Bonding in Water-Filled Carbon Nanotubes. *J. Am. Chem. Soc.* **128**, 12090–12097 (2006).
16. Kyakuno, H. *et al.* Confined water inside single-walled carbon nanotubes: Global phase diagram and effect of finite length. *The Journal of Chemical Physics* **134**, 244501 (2011).
17. Ohba, T. Size-Dependent Water Structures in Carbon Nanotubes. *Angewandte Chemie International Edition* **53**, 8032–8036 (2014).
18. Dalla Bernardina, S. *et al.* Water in Carbon Nanotubes: The Peculiar Hydrogen Bond Network Revealed by Infrared Spectroscopy. *J. Am. Chem. Soc.* **138**, 10437–10443 (2016).
19. Agrawal, K. V., Shimizu, S., Draushuk, L. W., Kilcoyne, D. & Strano, M. S. Observation of extreme phase transition temperatures of water confined inside isolated carbon nanotubes. *Nature Nanotech* **12**, 267–273 (2017).

20. Ye, H., Naguib, N. & Gogotsi, Y. TEM Study of Water in Carbon Nanotubes. *JEOL News* **39**, 38–43 (2004).
21. Martí, J. & Gordillo, M. C. Effects of confinement on the vibrational spectra of liquid water adsorbed in carbon nanotubes. *Phys. Rev. B* **63**, 165430 (2001).
22. Koga, K., Gao, G. T., Tanaka, H. & Zeng, X. C. Formation of ordered ice nanotubes inside carbon nanotubes. *Nature* **412**, 802–805 (2001).
23. Mashl, R. J., Joseph, S., Aluru, N. R. & Jakobsson, E. Anomalous Immobilized Water: A New Water Phase Induced by Confinement in Nanotubes. *Nano Lett.* **3**, 589–592 (2003).
24. Wang, J., Zhu, Y., Zhou, J. & Lu, X.-H. Diameter and helicity effects on static properties of water molecules confined in carbon nanotubes. *Phys. Chem. Chem. Phys.* **6**, 829–835 (2004).
25. Souza, N. R. de, Kolesnikov, A. I., Burnham, C. J. & Loong, C.-K. Structure and dynamics of water confined in single-wall carbon nanotubes. *J. Phys.: Condens. Matter* **18**, S2321 (2006).
26. Cicero, G., Grossman, J. C., Schwegler, E., Gygi, F. & Galli, G. Water Confined in Nanotubes and between Graphene Sheets: A First Principle Study. *J. Am. Chem. Soc.* **130**, 1871–1878 (2008).
27. Thomas, J. A. & McGaughey, A. J. H. Water Flow in Carbon Nanotubes: Transition to Subcontinuum Transport. *Phys. Rev. Lett.* **102**, 184502 (2009).
28. Pascal, T. A., Goddard, W. A. & Jung, Y. Entropy and the driving force for the filling of carbon nanotubes with water. *Proceedings of the National Academy of Sciences* **108**, 11794–11798 (2011).
29. Liang, C., Rayabharam, A. & Aluru, N. R. Structural and Dynamical Properties of H₂O and D₂O under Confinement. *J. Phys. Chem. B* **127**, 6532–6542 (2023).
30. Calegari Andrade, M. F. & Pham, T. A. Probing Confinement Effects on the Infrared Spectra of Water with Deep Potential Molecular Dynamics Simulations. *J. Phys. Chem. Lett.* **14**, 5560–5566 (2023).
31. Darling, B. T. & Dennison, D. M. The Water Vapor Molecule. *Phys. Rev.* **57**, 128–139 (1940).
32. Gordillo, M. C. & Martí, J. Hydrogen bond structure of liquid water confined in nanotubes. *Chemical Physics Letters* **329**, 341–345 (2000).
33. Alexiadis, A. & Kassinos, S. Influence of water model and nanotube rigidity on the density of water in carbon nanotubes. *Chemical Engineering Science* **63**, 2793–2797 (2008).
34. Joseph, S. & Aluru, N. R. Why Are Carbon Nanotubes Fast Transporters of Water? *Nano Lett.* **8**, 452–458 (2008).
35. Tao, J., Song, X., Zhao, T., Zhao, S. & Liu, H. Confinement effect on water transport in CNT membranes. *Chemical Engineering Science* **192**, 1252–1259 (2018).
36. Krivanek, O. L. *et al.* Progress in ultrahigh energy resolution EELS. *Ultramicroscopy* **203**, 60–67 (2019).
37. Hage, F. S., Kepaptsoglou, D. M., Ramasse, Q. M. & Allen, L. J. Phonon Spectroscopy at Atomic Resolution. *Phys. Rev. Lett.* **122**, 016103 (2019).
38. Rez, P. *et al.* Damage-free vibrational spectroscopy of biological materials in the electron microscope. *Nature Communications* **7**, 10945 (2016).
39. Haiber, D. M. & Crozier, P. A. Nanoscale Probing of Local Hydrogen Heterogeneity in Disordered Carbon Nitrides with Vibrational Electron Energy-Loss Spectroscopy. *ACS Nano* **12**, 5463–5472 (2018).
40. Hachtel, J. A. *et al.* Identification of site-specific isotopic labels by vibrational spectroscopy in the electron microscope. *Science* **363**, 525–528 (2019).

41. Hachtel, J. A. *et al.* A New Path to Nanoscale Cellular Analysis with Monochromated Electron Energy-Loss Spectroscopy. Preprint at <https://doi.org/10.48550/arXiv.2206.04191> (2022).
42. Jokisaari, J. R. *et al.* Vibrational Spectroscopy of Water with High Spatial Resolution. *Advanced Materials* **30**, 1802702 (2018).
43. Crozier, P. A. Vibrational and valence aloof beam EELS: A potential tool for nondestructive characterization of nanoparticle surfaces. *Ultramicroscopy* **180**, 104–114 (2017).
44. Travalloni, L., Castier, M., Tavares, F. W. & Sandler, S. I. Critical behavior of pure confined fluids from an extension of the van der Waals equation of state. *The Journal of Supercritical Fluids* **55**, 455–461 (2010).
45. Hudait, A. & Molinero, V. Ice Crystallization in Ultrafine Water–Salt Aerosols: Nucleation, Ice-Solution Equilibrium, and Internal Structure. *J. Am. Chem. Soc.* **136**, 8081–8093 (2014).
46. Malfait, B. *et al.* Structure of Water at Hydrophilic and Hydrophobic Interfaces: Raman Spectroscopy of Water Confined in Periodic Mesoporous (Organo)Silicas. *J. Phys. Chem. C* **126**, 3520–3531 (2022).
47. Krivanek, O. L. *et al.* Probing Biological Materials by Vibrational Analysis in the Electron Microscope. *Microscopy and Microanalysis* **28**, 1196–1197 (2022).
48. Takaiwa, D., Hatano, I., Koga, K. & Tanaka, H. Phase diagram of water in carbon nanotubes. *Proceedings of the National Academy of Sciences* **105**, 39–43 (2008).

Methods

Sample Preparation: SiN_x liquid cells were K-kit (Silicon-based Micro Channel Device) purchased from Electron Microscopy Sciences (EMS) with membrane thickness of 30 nm and gap height of 100 nm. The liquid cells were opened, filled with DI water, and sealed with TorrSeal following the instructions provided by EMS. CNTs were directly grown as described previously¹ except on holey SiN_x TEM grids (500 nm or 200 nm pore (21583-10 or 21586-10 respectively, TED Pella) using a low gas flow variant² of a chemical vapor deposition (CVD) method that results in a sparse array of gas flow-aligned ultralong CNTs³. For this work, CH₄ was utilized as a carbon precursor and iron particles contained in 25 Series APT Carbon Nanotubes from Nano-C were used as catalysts. For this, a CNT dispersion is produced as described elsewhere⁴, then drop cast onto the upstream side of the growth substrate. Substrates were placed in a tube furnace during growth in a manner such that the catalyst was located upstream of the holey SiN_x membrane so that the synthesized ultralong CNTs cross the TEM grid and suspended across its windows. After CVD synthesis, the CNTs were then subjected to a previously introduced Focused Ion Beam (FIB) cutting procedure to induce CNT opening^{5,6}. Briefly, the focused Ga⁺ beam of a dual beam FIB/scanning electron microscope (FEI Helios Nanolab 600) is used to cut the ultralong CNTs between the catalyst and TEM window and once beyond the same window. We use the following FIB patterning parameters: 9 pA, 30 kV, 100 passes, 5 μs dwell time, and 4 nm pitch. Any exposure of the membrane-supported CNT segments in between the two cut locations to electron or ion beams was carefully avoided. The CNTs were then transported and exposed to above 99% RH conditions in a custom-built humidity chamber (Supplementary Fig. S1a) using an ultrasonic humidifier as a standardized water filling process. We subsequently applied TorrSeal (Agilent Technologies) to the two FIB-cut regions of the sample (Supplementary Fig. S1b), again avoiding

the region between, as a CNT sealing method. Distinctive, temperature dependent Raman RBM trajectories were observed for CNTs before and after the water filling process, as described elsewhere⁶.

Transmission Electron Microscopy: TEM images were acquired on an FEI Titan 80-300 environmental transmission electron microscope operated at 80 kV, with an aberration corrector for the objective lens tuned before each session. The electron dose rate during HRTEM image acquisitions was measured at $\sim 300 \text{ e}^-/\text{\AA}^2/\text{s}$. TEM images were analyzed using GATAN DigitalMicrograph and ImageJ software.

Vibrational Electron Energy Loss Spectroscopy: The vibrational EELS in this manuscript is acquired with the Nion high energy-resolution monochromated EELS-STEM (HERMES) located at Oak Ridge National Laboratory. The spectra shown here are acquired from different experimental sessions, operating at both 60 kV and 30 kV accelerating voltages. However, the 1.4-nm-diameter CNT and the 2.3-nm-diameter CNT are acquired from the same sample during the same session (accelerating voltage 60 kV) to insure minimum experimental variance. All spectra acquired with a convergence angle of 30 mrad and a collection angle of 25 mrad. Energy resolutions for these acquisitions varied from 8-15 meV. The beam current for these experiments monochromation is approximately 4 pA, and while acquiring reference images to prepare spectrum images or point spectra, dwell times are kept extremely low to minimize sample irradiation. Due to the presence of the combination bands, we focus exclusively on the region between 350 meV and 500 meV to highlight the behavior of the O-H stretching. Bands of vibrations both below and above the O-H stretch are observed in the filled CNT system that are not present in the bulk-water liquid cell measurements or the empty CNT that we assign to combination bands, as explained in Supplementary Discussion 1. Also due to the presence of combination bands and the conductive continuum present in the spectra, a number of different background normalization methodologies are implied. Full details and validation of all background subtraction and quantitative normalization methodologies, as well as the energy resolution of each spectrum and spectrum image shown in this manuscript is tabulated in Supplementary Discussion 3. All experiments are conducted in ultrahigh vacuum which minimizes ice build up during cryo-experiments. The lack of ice-like peaks in the 1.4-nm-diameter CNT cryo experiment shown in Fig. 3a serves as proof that ice is not building up significantly during the experiments.

DFT calculations: We performed density-functional-theory molecular-dynamics (DFT-MD) simulations for water confined in carbon nanotube (CNT) using the Vienna ab initio simulation package (VASP)⁷⁻⁹ and the projected augmented wave (PAW) method^{10,11}. The exchange-correlation functional for electrons was described by the generalized gradient approximation (GGA) in the Perdew-Burke-Ernzerhof (PBE) form¹² and the Grimme D3 method was included to describe van der Waals (vdW) interactions¹³. The PBE-D3 functional has been validated as

showing very good performance in describing the water-water and water-CNT interactions while keeping a reasonable computational-resources cost^{14,15}.

It is known that for water, the DFT description of properties is affected by the choice of functional. To further assess the effects of the functional choice on our key results, we also calculated the vDOS and d_{00}/θ heatmap of water/CNT (water density $\rho=0.5$ g/cm³, CNT diameter 1.1 nm) using two additional functionals: PBE-D4, which uses the Gimme D4 version of the van der Waals contribution, and TPSS-D4, which is a computationally expensive meta-GGA functional. The three functionals have previously been found to be the best-performing functionals for water/CNT systems within each functional class^{14,15}. The calculated room-temperature vDOS and d_{00}/θ heatmaps using the three different functionals are very similar to each other, as shown in Supplementary Fig. S12 and S15, demonstrating the effectiveness of the PBE-D3 functional for our purposes. Additionally, the low-temperature (100 K) vDOS and d_{00}/θ heatmaps of water/CNT at different water densities ($\rho=0.4, 0.45, \text{ and } 0.5$ g/cm³) were also calculated using PBE-D3 and TPSS-D4 functionals (PBE-D4 always gives the same results as the PBE-D3). As shown in Supplementary Fig. S15a, at $\rho=0.5$ g/cm³, the TPSS-D4-calculated vDOS exhibits two peaks, differing from the PBE-D3 vDOS and the cryo-vEELS. However, when the density is further decreased to 0.45 g/cm³ or lower (Supplementary Fig. S15b, c), the vDOS calculated by PBE-D3 and TPSS-D4 are quite similar and consistent with the cryogenic experiment.

The plane-wave cutoff was set as 400 eV and a Γ -centered ($1\times 1\times 1$) k-mesh was applied for all the calculations. A (8,8) single-walled CNT (diameter 1.1 nm) with length of 1.9 nm was used to simulate the medium-diameter CNT used in experiments, while other cases, including a (10, 10) single-walled CNT (diameter 1.4 nm) and a (8,8)@(13,13) double-walled CNT (outer diameter 1.7 nm) were also studied to check the effect of CNT diameter and outer wall. The effect of the CNT length on the confined water VDOS was also checked and found there very little different between the VDOS calculated by 1.9 and 2.9 nm long CNT, as shown in Fig. S16. Periodic boundary conditions were applied along the axis-direction (z -direction), while a vacuum distance larger than 10 Å was set along the in-plane direction to separate the periodic neighbor.

The density of water in a CNT is defined as the ratio of the mass of water molecules and the volume of the CNT, estimated by removing a 2-Å-wide shell from the CNT radius defined by the carbon nuclei. In order to control the computational costs, we used a fixed CNT length (see above) and controlled the water density by changing the number of molecules. Water densities of 1.5, 1.0, 0.75 and 0.5 g/cm³ cases, were studied by including 36, 24, 18 and 12 water molecules into the (8,8) CNT, where the initial configurations of water molecules were random. In the case of 12 water molecules, we tested the statistical accuracy of the number by performing simulations for 18 molecules in a CNT that was 1.5 times longer.

Then 10 ps DFT-MD simulations with time step of 0.5 fs were performed at both 300 K and 100 K using the Nosé algorithm^{16,17}, for both rigid-CNT and vibrating-CNT cases. The vibrational densities of states of the confined water were obtained through Fourier transform of the velocity

autocorrelation function^{18,19} of the H and O atoms by using VASPKIT²⁰. The frequency and d_{oo}/θ heatmap was calculated by taking two water molecules as a model, as shown schematically in Supplementary Fig. S7m (top panel), where only the H atom between the two O atoms was allowed to vibrate, while other atoms were kept fixed.

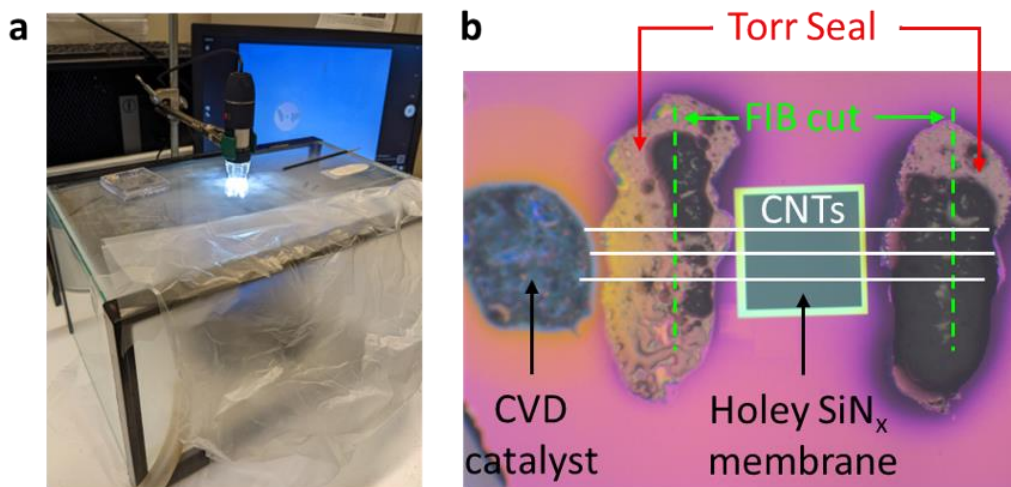
Methods References

1. Agrawal, K. V., Shimizu, S., Drahushuk, L. W., Kilcoyne, D. & Strano, M. S. Observation of extreme phase transition temperatures of water confined inside isolated carbon nanotubes. *Nature Nanotech* **12**, 267–273 (2017).
2. Jin, Z. *et al.* Ultralow Feeding Gas Flow Guiding Growth of Large-Scale Horizontally Aligned Single-Walled Carbon Nanotube Arrays. *Nano Lett.* **7**, 2073–2079 (2007).
3. Huang, S., Cai, X. & Liu, J. Growth of Millimeter-Long and Horizontally Aligned Single-Walled Carbon Nanotubes on Flat Substrates. *J. Am. Chem. Soc.* **125**, 5636–5637 (2003).
4. Jain, R. M. *et al.* Polymer-Free Near-Infrared Photovoltaics with Single Chirality (6,5) Semiconducting Carbon Nanotube Active Layers. *Advanced Materials* **24**, 4436–4439 (2012).
5. Kuehne, M. *et al.* Impedance of Thermal Conduction from Nanoconfined Water in Carbon Nanotube Single-Digit Nanopores. *J. Phys. Chem. C* **125**, 25717–25728 (2021).
6. Faucher, S. *et al.* Observation and Isochoric Thermodynamic Analysis of Partially Water-Filled 1.32 and 1.45 nm Diameter Carbon Nanotubes. *Nano Lett.* **23**, 389–397 (2023).
7. Kresse, G. & Furthmüller, J. Efficiency of ab-initio total energy calculations for metals and semiconductors using a plane-wave basis set. *Computational Materials Science* **6**, 15–50 (1996).
8. Kresse, G. & Hafner, J. Ab initio molecular dynamics for liquid metals. *Phys. Rev. B* **47**, 558–561 (1993).
9. Kresse, G. & Hafner, J. Ab initio molecular dynamics for open-shell transition metals. *Phys. Rev. B* **48**, 13115–13118 (1993).
10. Blochl, P. E. Projector Augmented-Wave Method. *Phys. Rev. B* **50**, 17953–17979 (1994).
11. Kresse, G. & Joubert, D. From ultrasoft pseudopotentials to the projector augmented-wave method. *Phys. Rev. B* **59**, 1758–1775 (1999).
12. Perdew, J. P., Burke, K. & Ernzerhof, M. Generalized Gradient Approximation Made Simple. *Phys. Rev. Lett.* **77**, 3865–3868 (1996).
13. Grimme, S., Antony, J., Ehrlich, S. & Krieg, H. A consistent and accurate ab initio parametrization of density functional dispersion correction (DFT-D) for the 94 elements H-Pu. *The Journal of Chemical Physics* **132**, 154104 (2010).
14. Gillan, M. J., Alfè, D. & Michaelides, A. Perspective: How good is DFT for water? *The Journal of Chemical Physics* **144**, 130901 (2016).
15. Brandenburg, J. G., Zen, A., Alfè, D. & Michaelides, A. Interaction between water and carbon nanostructures: How good are current density functional approximations? *The Journal of Chemical Physics* **151**, 164702 (2019).
16. Nosé, S. A molecular dynamics method for simulations in the canonical ensemble. *Molecular Physics* **52**, 255–268 (1984).
17. Nosé, S. A unified formulation of the constant temperature molecular dynamics methods. *The Journal of Chemical Physics* **81**, 511–519 (1984).
18. DICKEY, J. M. & PASKIN, A. Computer Simulation of the Lattice Dynamics of Solids. *Phys. Rev.* **188**, 1407–1418 (1969).

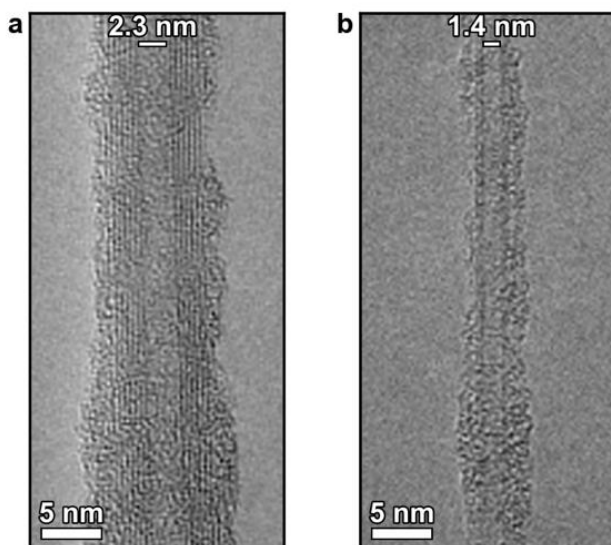
19. Lin, S.-T., Blanco, M. & Goddard, W. A., III. The two-phase model for calculating thermodynamic properties of liquids from molecular dynamics: Validation for the phase diagram of Lennard-Jones fluids. *The Journal of Chemical Physics* **119**, 11792–11805 (2003).
20. Wang, V., Xu, N., Liu, J.-C., Tang, G. & Geng, W.-T. VASPKIT: A user-friendly interface facilitating high-throughput computing and analysis using VASP code. *Computer Physics Communications* **267**, 108033 (2021).

Supplementary Information for The structure of highly confined water unveiled by nanoscale vibrational spectroscopy and simulations

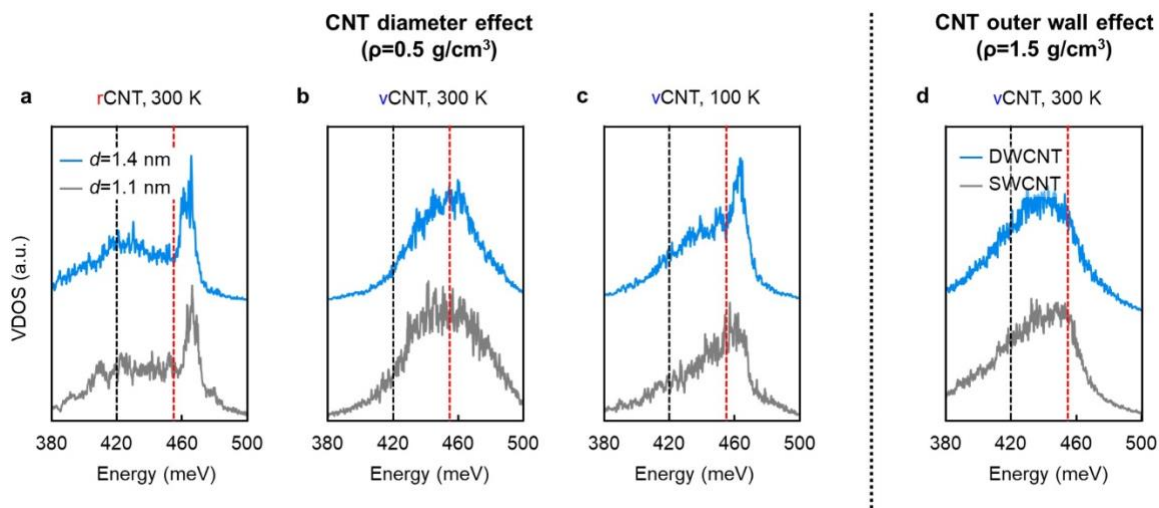
Supplementary Figures



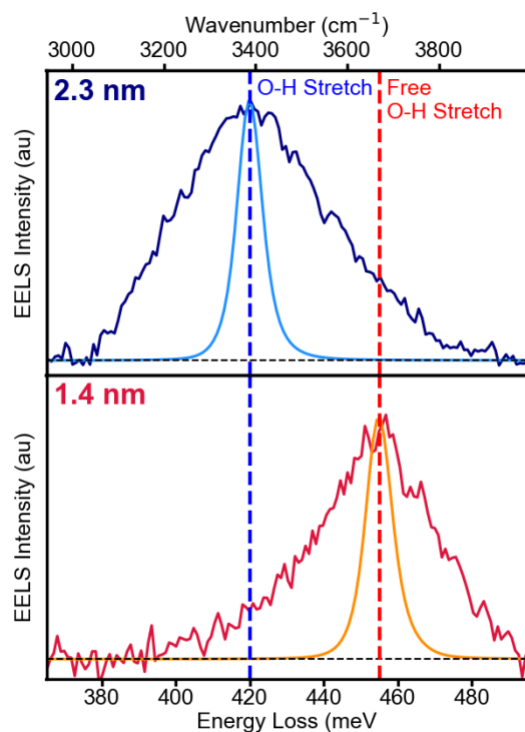
Supplementary Figure S1. Procedure for CNT water filling. (a) A custom-built humidity chamber with a microscope. (b) Optical micrograph of a holey SiN_x TEM chip after CVD growth and FIB cutting (along green dashed lines) of CNTs (schematically illustrated as continuous white lines) as well as their exposure to above 99% RH conditions and Torr Seal application. Note that Torr Seal covers the FIB cut regions but not the holey SiN_x membrane.



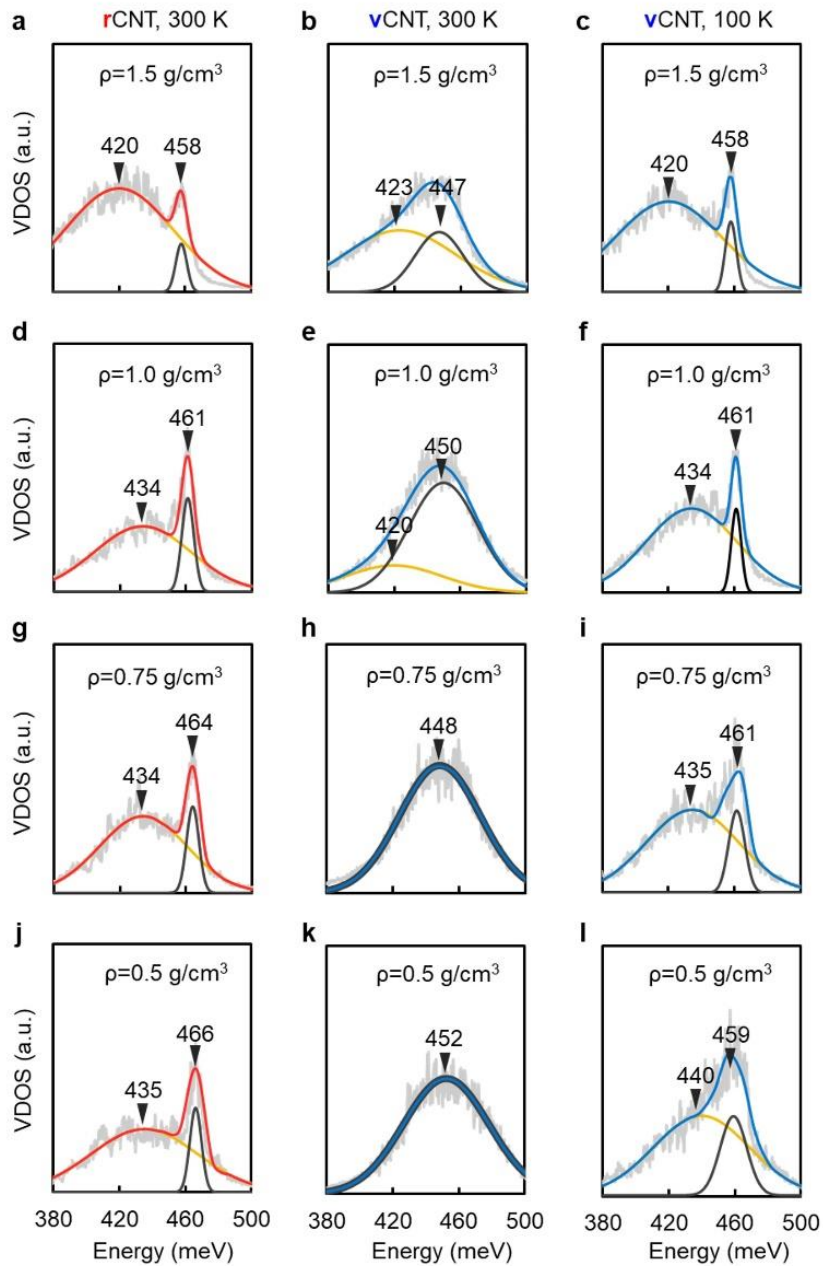
Supplementary Figure S2. Sample preparation. TEM images of the most examined CNTs in the main text with large and medium diameters. (a) The filled large-diameter tube from Fig. 1d-h, Fig. 2a, and Fig. 3a is measured to have an average inner diameter of ~2.3 nm. (b) The filled medium-diameter tube from Figs. 2a and 3a is measured to have an inner diameter of ~1.4 nm.



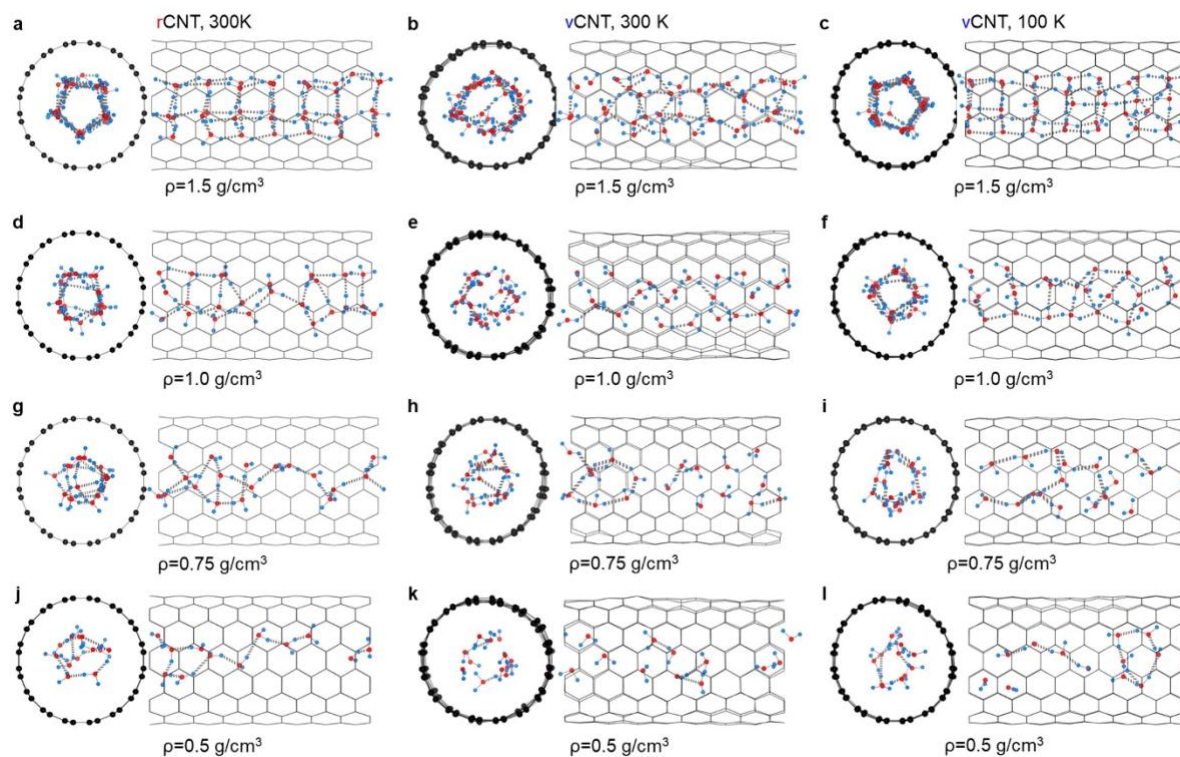
Supplementary Figure S3. VDOS of water confined in single-wall CNT (SWCNT) with larger diameter ($d=1.4$ nm) and double wall CNT (DWCNT). (a)-(c): VDOS of water confined in rigid- and vibrating-SWCNT with diameter 1.4 nm at 300 K and 100 K. The VDOS of the 1.4 nm CNT for both the rigid and vibrating cases compare very well with the corresponding vDOS of the 1.1 nm CNT. The density of the confined water is 0.5 g/cm³. (d) Demonstration that a vibrating double-wall CNT behaves the same way as a vibrating single-wall CNT. The density of the confined water is 1.5 g/cm³.



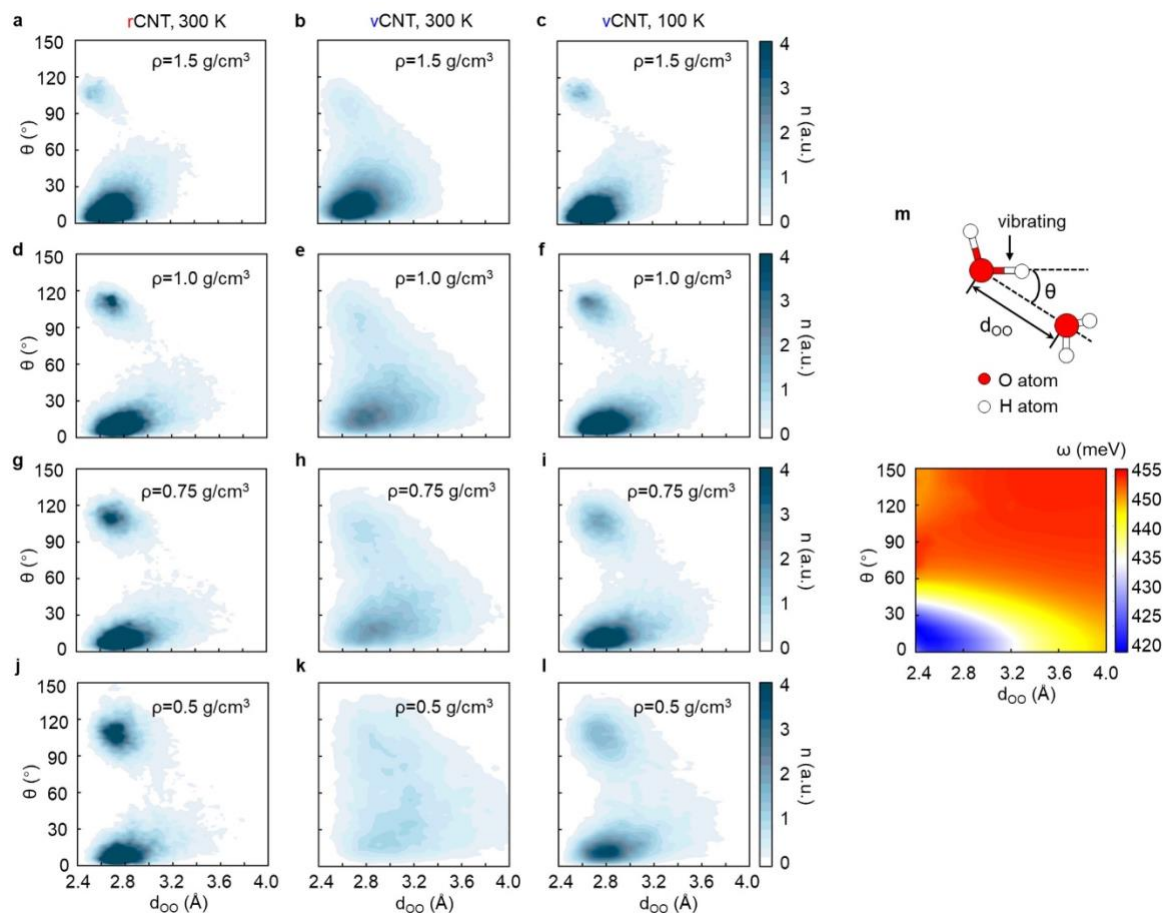
Supplementary Figure S4. Instrumental broadening vs. Spectral Linewidth. In this figure we show that our instrumental resolution is significantly below the measured linewidth of the vibrational spectra for the vibrational spectra shown in the large (2.3 nm) diameter tube and the smaller (1.4 nm) diameter tube from the main text figures. For the 2.3 nm tube the full-width at half-maximum (FWHM) of the O-H stretch is 50.1 meV, while the FWHM of the 1.4 nm tube is 34.0 meV. For all EEL spectra the energy resolution can be quantified by measuring the FWHM of the zero-loss peak (ZLP), which corresponds to all electrons in the EEL that have either elastically scattered off the sample or not interacted with the sample at all. As a result, this peak represents the spread of electron energies in the beam with which all peaks are convolved with and represents the instrumental broadening. For both spectra the FWHM of the ZLP is 8.5 meV, indicating that the vibrational peak width is dominated by the native linewidth of the peak, not instrumental broadening.



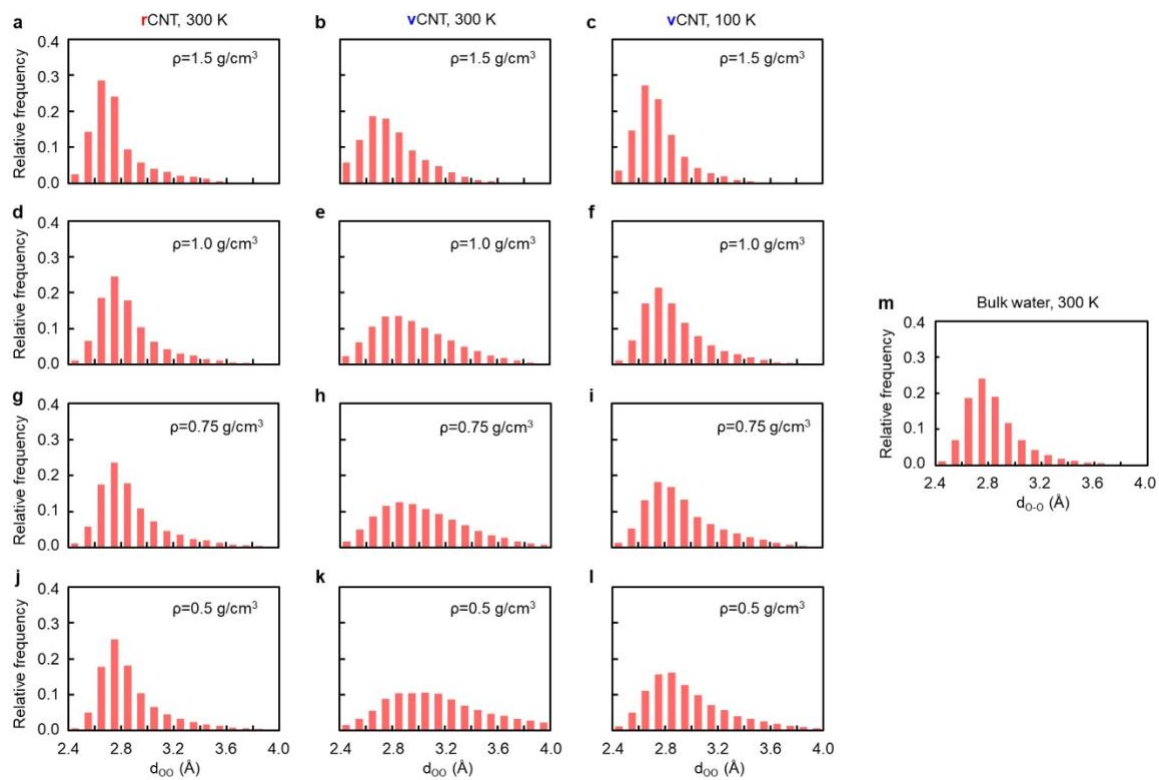
Supplementary Figure S5. VDOS of water/CNT ($d=1.1 \text{ nm}$) at different densities and temperatures as indicated. Here the VDOS are deconvoluted by two Gaussian peaks, shown in yellow and black colors. The centers of the two peaks are marked by the numbers. We note, here the two Gaussian peaks can be used to estimate the ratio between the high and low frequency component (centered at ~ 455 and ~ 420 meV, respectively) in the VDOS.



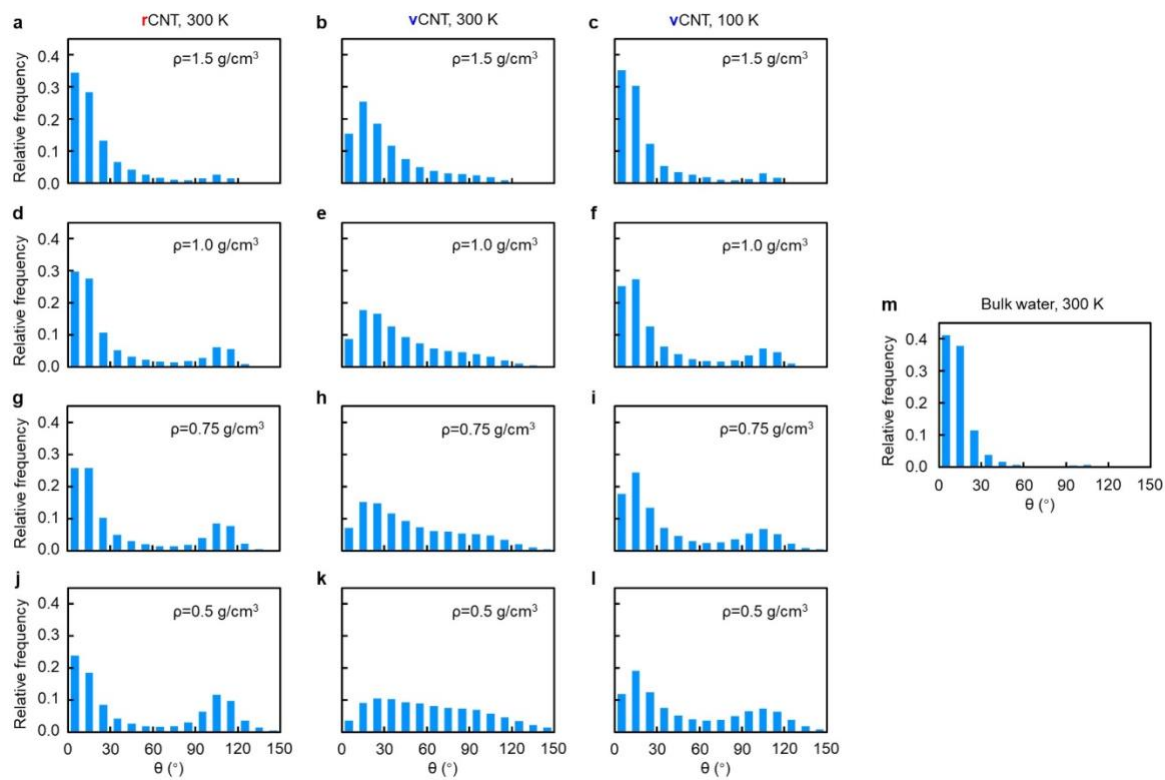
Supplementary Figure S6. MD Snapshots from Simulations. Axial and cross-sectional snapshots of the MD simulations at as-labeled water densities and temperatures. In each snapshot, intermolecular H \cdots O bonds are highlighted by dashed lines. Here, we see that, even for the higher densities, the CNT vibrations cause significant disruption of the H-bond network and the formation of more ‘free’ O-H bonds. Red atoms are oxygen and blue atoms are hydrogen.



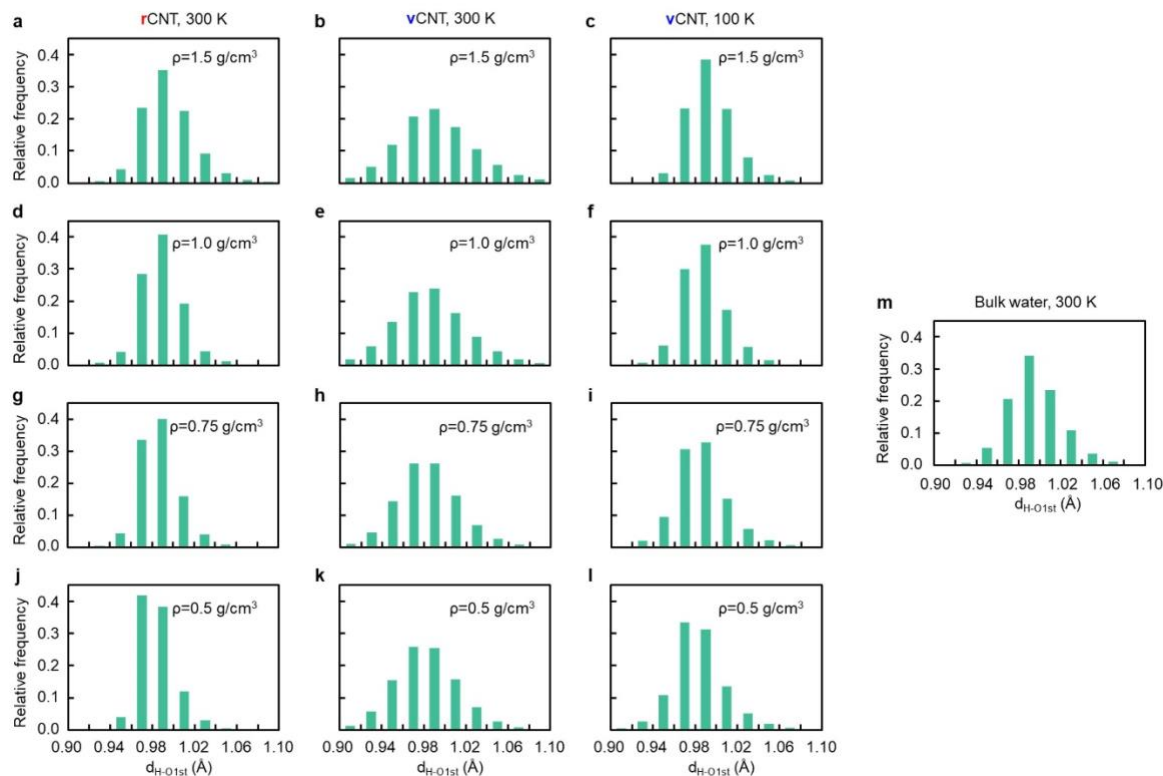
Supplementary Figure S7. Statistical heatmaps from Simulations. (a-l) d_{oo}/θ heatmaps from MD simulations for the as labeled water densities and temperatures (the color bars are normalized to be quantitatively comparable to one another). The values plotted in the heat maps are obtained from molecules in all the snapshots of the corresponding MD simulations. (m) Top panel shows a schematic of the nearest-neighbor molecular structure used to define d_{oo} and θ the heatmaps in (a-l) and the O-H stretch frequency ω as a functional of d_{oo} and θ . Since the color map in panel m is constructed using the two-water molecule model, it is only qualitatively indicative of the frequencies that correspond to the heat maps in panels a-l.



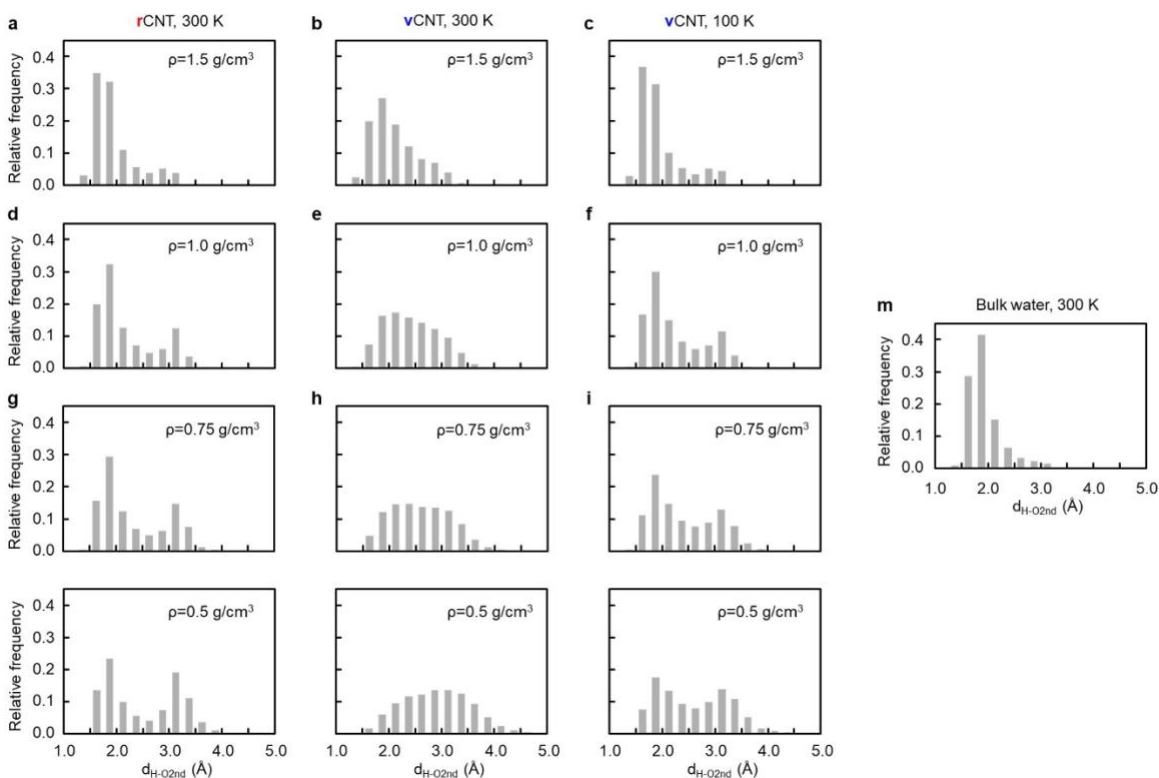
Supplementary Figure S8. H-O-O angle θ as defined in Fig. S7m. θ distribution histogram of water confined in CNT ($d=1.1$ nm) for all the densities and temperatures presented in the main text and SI.



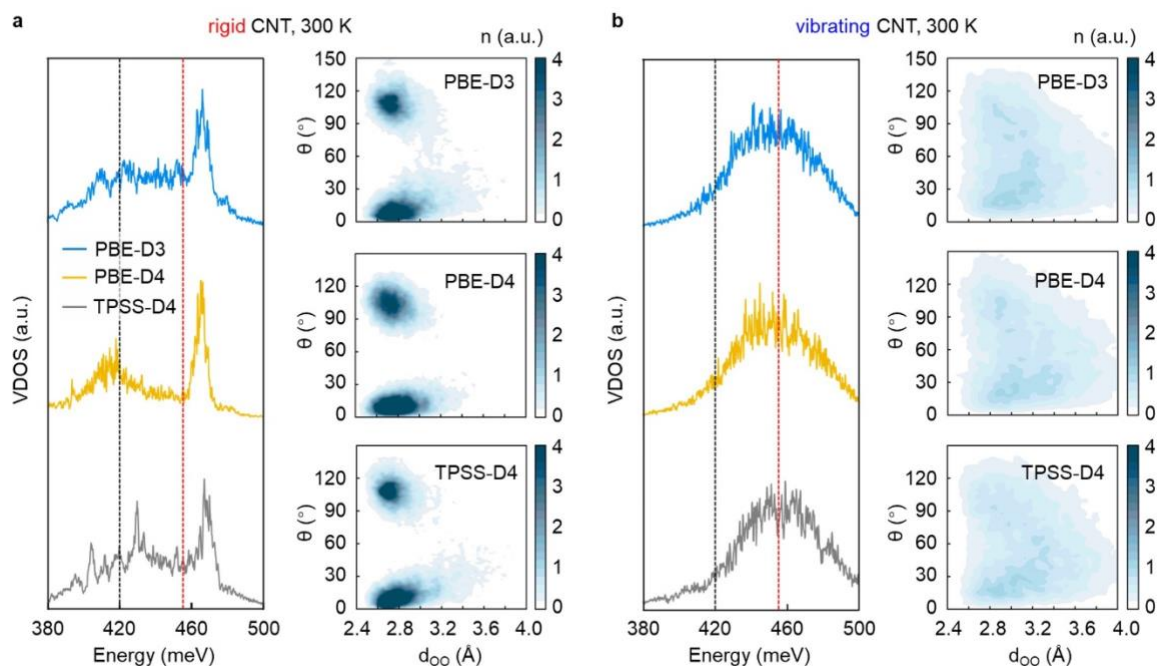
Supplementary Figure S9. Oxygen-oxygen d_{O-O} . d_{O-O} distribution histogram of water confined in CNT ($d=1.1 \text{ nm}$) for all the densities and temperatures presented in the main text and SI.



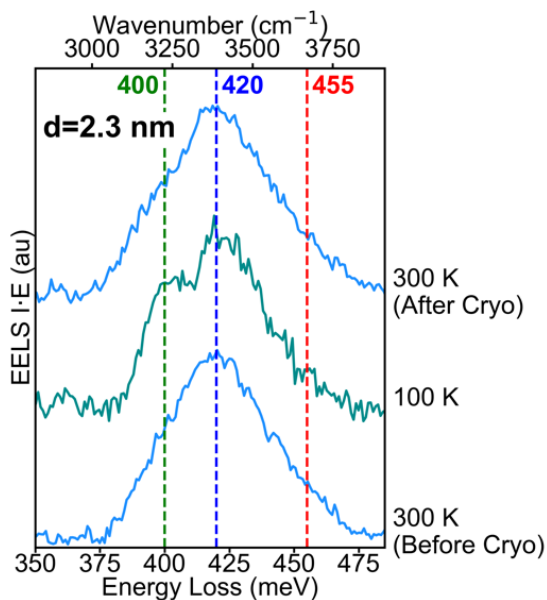
Supplementary Figure S10. O-H bond lengths. d_{H-O1st} distribution histogram of water confined in CNT ($d=1.1$ nm) for all the densities and temperatures presented in the main text and SI. Here, O_{1st} represents the oxygen atom closest to the H atom, as in the oxygen atom on the same molecule as the H-atom. These are the *intramolecular* O-H bonds. These calculations critically show while there is some change in the variation of the O-H bond length as a function of tube vibration the average length remains unchanged (~ 0.98 Å).



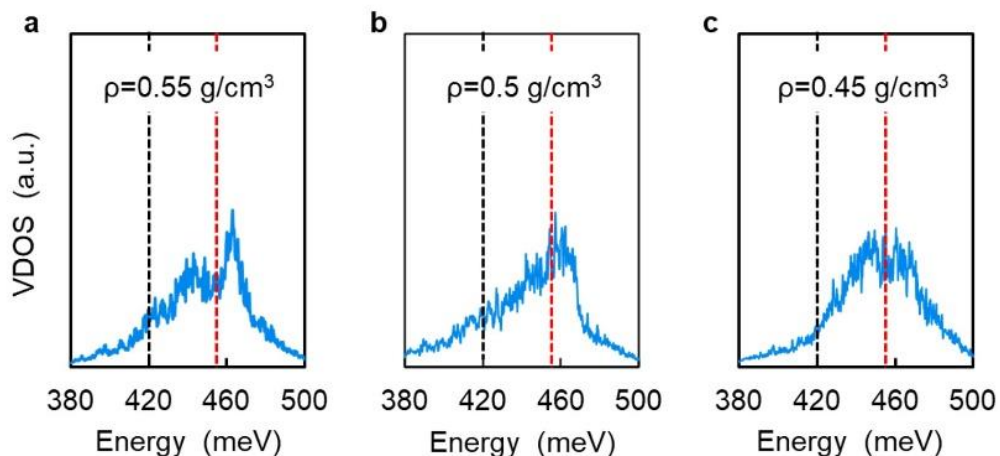
Supplementary Figure S11. H-O bond lengths. d_{H-O2nd} distribution histogram of water confined in CNT ($d=1.1$ nm) for all the densities and temperatures presented in the main text. Here, O_{2nd} represents the second closest oxygen atom to the H atom, as in the oxygen atom on the nearest neighbor molecule. These are the *intermolecular* O-H bonds. These simulations show the same split between bimodal and singular distributions due to disordering induced by the CNT vibrations as the heat maps in the main text.



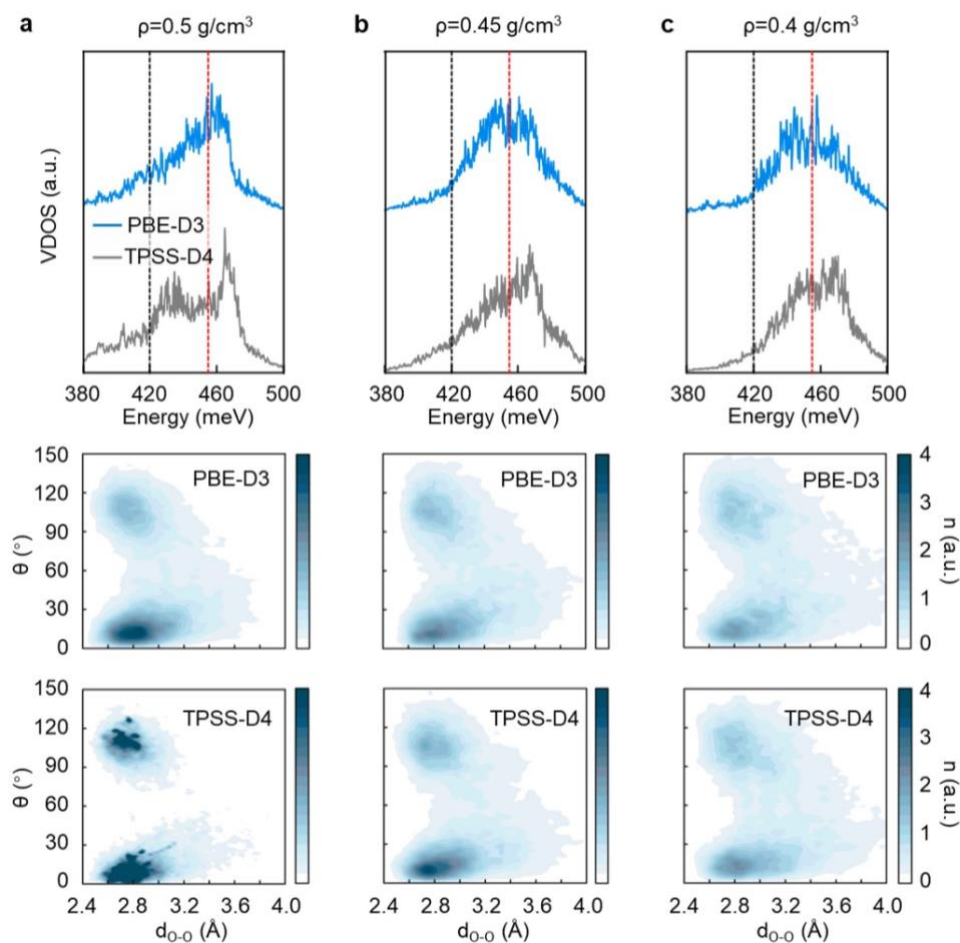
Supplementary Figure S12. Room temperature VDOS and d_{oo}/θ map of water confined in rigid/vibrating-CNT (diameter 1.1 nm) calculated using different functionals. The density of the confined water is 0.5 g/cm^3 in all the cases. The calculated VDOS and heat map using three different functionals are quite similar to each other, demonstrating the choice of functionals has minimal effects on the structure and properties of the confined water.



Supplementary Figure S13. Reversibility of the crystalline phase change. vEELS on the 2.3-nm-diameter CNT for a full cryo-cycle, meaning measurements at 300 K, 100 K, then back to 300 K, showing the emergence and disappearance of a ice-like peak at 400 meV.



Supplementary Figure S14. Density-dependent evolution of the cryogenic vibrational spectrum. vDOS at 100 K for three different water densities showing that $\rho = 0.5 \text{ g/cm}^3$ is the critical water density for which a single peak is observed in the vibrational DOS (indicating that the non-H-bonded water phase persists) at 100 K. These differences show that small differences in the density ($\sim 0.05 \text{ g/cm}^3$) can significantly impact the resulting vibrational response.

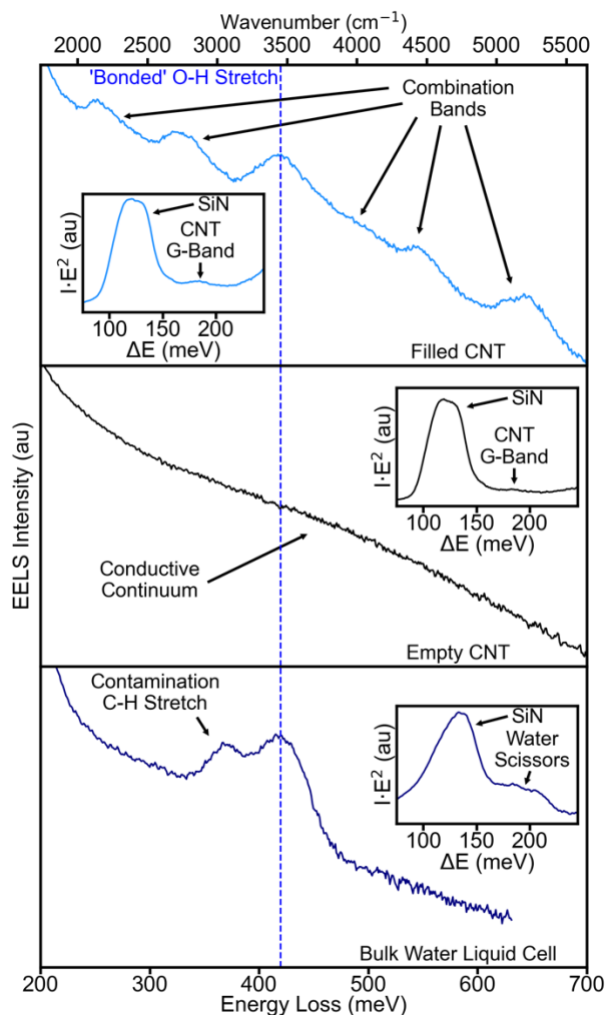


Supplementary Figure S15. Low temperature (100 K) vDOS and d_{oo}/θ map of water confined in vibrating-CNT (diameter 1.1 nm) calculated using different functionals. The densities of the confined water are 0.5, 0.45 and 0.4 g/cm^3 for the three cases. The 100 K vDOS calculated by PBE-D3 and TPSS-D4 differ from each other when $\rho = 0.5 \text{ g/cm}^3$, but consistent with each other when the density further decreases.

Supplementary Discussion 1: Additional Peaks Outside of the O-H Stretch Regime

As stated in the main text, there are more peaks in the measured vibrational spectra aside from just the O-H stretching modes. We assign these peaks as combination bands as other IR absorption spectroscopy techniques, as well as other vEELS experiments on ice have reported peaks in these regimes^{1,2}. In the main text, we focus exclusively on the O-H stretch regime between 370-500 meV due to the presence of these additional bands. We have not rigorously determined the origin of these bands, but believe the response is largely consistent with combination bands/overtones. Here, we present additional discussion on these vibrational peaks. In Figure S16, we show the three spectra from the main text Figure 1 from a filled CNT (Top), an empty CNT (Middle), and the bulk liquid cell (Bottom). The vast difference between the filled tube and the empty tube is even more dramatic in the full range picture, with the empty tube showing absolutely no sharp features, and only a broad sloping continuum that is present in any amorphous/conductive material corresponding to low-energy electronic transitions. We also note that the empty CNT and the filled CNT are from the same sample, and hence prepared under identical conditions. This serves as a strong piece of evidence that the main 420 meV peak discussed in the main text, and the other bands are both originating from the water. The tube filling rate is not predicted to be 100%, so one being full and the other being empty is a highly likely scenario, and perhaps no other physical scenario could result in such a dramatic difference between the vibrational spectra.

In the comparison to bulk water in Fig. S16, the bonded O-H stretch matches well, but these other features do not. Analyzing bulk water is much more straightforward since larger scale volumes of water can be confined in liquid cells. Our comparison is done on a bulk liquid cell with a macroscopic volume of water confined between two SiN windows. Due to the dirty nature of the sample preparation, and our inability to perform standard contamination mitigation protocols (such as baking and plasma cleaning), a large amount of hydrocarbons accumulate

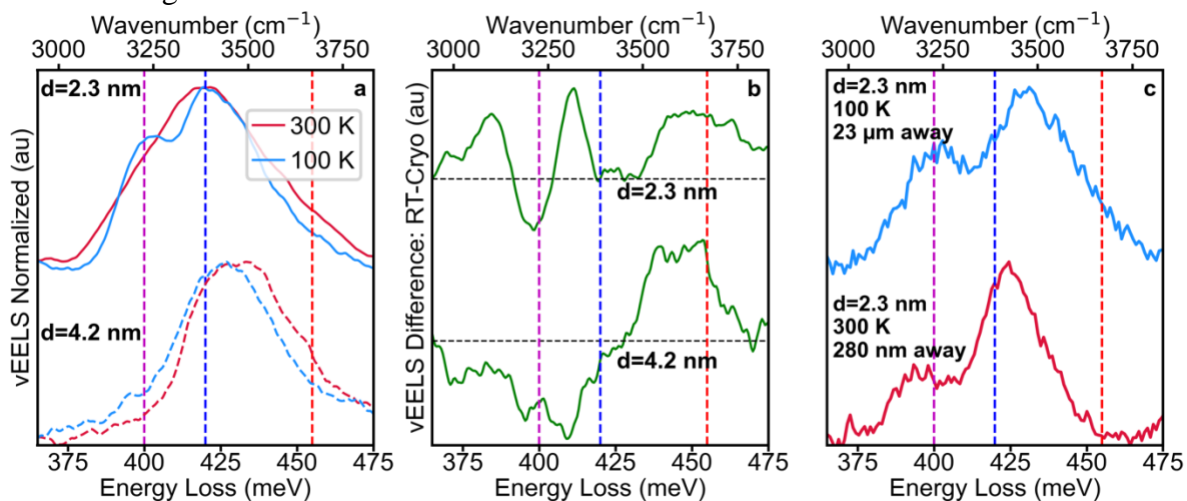


Supplementary Figure S16. Full vibrational spectrum of Filled CNT, Empty CNT, and Bulk Water. Here we show the full vibrational response of all three spectra shown in the main text of Figure 1. In each we show the spectrum in log-scale and in the inset we show the SiN/G-Band vibrations of the substrate/CNT. (Top) filled CNT, (Middle) Empty CNT, (Bottom) bulk liquid cell.

under the beam during acquisition. As a result, for the liquid cells we see two peaks, at 420 meV and 365 meV which are consistent with the O-H and C-H stretches respectively. In bulk water, we see no other peaks anywhere in the bulk water spectrum other than the C-H and O-H stretches, which is consistent with our previous work on the vibrational spectroscopy of water in graphene/h-BN liquid cells³. While this does not directly connect the additional peaks to combination bands, it directly connects the changed nature of the vibrational response to the confinement induced by the nanotube. Moreover, it shows that even in the case of a larger CNT diameter where the water shows the ‘bonded’ O-H stretch frequency of 420 meV, the vibrations in the water are still fundamentally different from those found bulk water. These peaks are in the spectral regime consistent with combination bands and potentially overtones of lower-frequency vibrations potentially indicating that the confinement of the CNT could increase the cross-section of these second order effects. However, this remains an open question that requires further validation and future study to understand better.

Supplementary Discussion 2: Repeatability of Temperature-Dependence Experiments

In the main text we present two cryogenic experiments, one for the 1.4 nm diameter tube and one for the 2.3-nm-diameter tube. We further go on to examine the reversibility of the phase transition in the 2.3-nm-diameter CNT in Figure S12. Each is summarized with two spectra, and more experiments were conducted to verify the repeatability of these measurements. Given the low filling rate of the CNTs, and a natural variance of the inner diameter of the tubes, finding filled tubes with similar diameters is challenging. Nevertheless, we managed to repeatedly observe both the 455 meV and the 420 meV peak phenomena on multiple independent tubes. We additionally take advantage of the length of the tubes (mm scale) to examine different parts of the same tubes. We report our observation as an initial experiment demonstrating the potential of vEELS (and especially cryo vEELS) and expect future development of new platforms for confined fluids will help obtain more robust analyses. A summary of our additional experiments is shown in Figure S17.



Supplementary Figure S17. Repeatability of phase change signatures in large diameter CNTs.

(a) Comparison of the room temperature (300 K) and cryogenic (100 K) spectra for the CNT shown in the main text and the other cryo experiment. (b) Difference spectra of the 300 K and 100 K spectra for each CNT. (c) shows other measurements on the 2.3 nm CNT. The top (blue) spectra shows a cryo measurement conducted many microns away from the original position of the spectra and the bottom (red) spectra shows a room-temperature measurement very close

We compare the results of the 2.3-nm-diameter CNT examined in the main text, to a larger 4.2-nm-diameter CNT in Fig. S17a and S17 b. On first glance, the 4.2 nm CNT does not appear to exhibit a significant phase change, as the peak has not changed in line-shape to nearly the same extent as the in the lower diameter tube. However, by normalizing the spectra and taking the difference (300 K spectrum minus the 100 K spectrum) we can see there is a strong similarity between the two experiments. Both have exhibited an overall redshift at cryogenic temperatures, as evidenced by the dip in intensities at around 400 meV and the increase in intensities at 455 meV. While the distinct 400 meV feature (corresponding to Ih ice) is less pronounced in the 4.2-nm-diameter CNT, this could easily be a factor of different phases of ice with different frequencies being present, or different ratios of crystalline and amorphous phases due to the difference in diameter.

The other piece of evidence that the phase change in the 2.3 nm tube is genuine is obtained by examining a position on the same CNT under cryogenic conditions very far away from the original spot. Figure S17c shows such a spectrum on the top, which exhibits a clear bimodal distribution with peaks near the 400 meV and 420 meV observed in the main text spectra. The ability to go so far away from the initial position and return a spectrum so similar to the initial spectrum is encouraging that these peaks are genuine features of the water inside the tube. It is important to note, that the bottom spectrum in Fig. S17c shows a room temperature spectrum from the CNT extremely close to where the original room temperature spectrum from Fig. S17a and all the main text figures is obtained, that shows a slight peak at 400 meV. The peak is much lower in intensity compared to the cryogenic spectrum, and peaks at both 400 meV and 420 meV have been observed room temperature water through vibrational sum frequency spectroscopy⁴, all of which still indicates that the reversible phase change shown for the 2.3-nm-diameter CNT does correspond to crystalline ice formation. However, this observation highlights the necessity to discuss potential artifacts that could influence our analysis. Contamination from hydrocarbons and combination bands have already been discussed Supplementary Discussion 1, however, beam-induced irradiation is possibly the largest potential for artifacts in our system.

We note that experiments were conducted in a mindset of limiting total exposure of the CNTs to the electron beam at all time, however, it is not possible to identify CNTs and align images without subjecting the areas to a small amount of electron dose before the initial acquisition. As a result radiolysis byproducts are certainly produced to some extent the electron beam interacting with the water⁵. By returning to the same positions we risk the possibility of dose directly driving the emergence of the 400 meV peak, and we cannot disprove this conjecture directly. However, in addition to the reversibility of the 400 meV peak emergence (highlighted in Fig. S13) the top spectrum in Fig. S17c shows the 400 meV and 420 meV peaks (both extremely pronounced) in a brand new area of the tube that had not been exposed to the electron beam, so we know it is not solely driven by beam irradiation.

Additionally, many other effects, such as the rate of cooling, or tensioning in the nanotube, or impurities in the confined water, or defects in the CNT, could also influence phase changes in confined fluids. We believe this result to be a powerful demonstration of the potential to monitor phase changes using vEELS, but to conclusively link the cryogenic phase changes (or lack thereof) identified through vEELS to specific physical origins and mechanisms, extensive statistics and follow up experiments controlling these variables will be needed. More controllable nanofluidic platforms and cooling processes that can be integrated with the vEELS workflow would be very helpful in future studies of phase transitions in fluids.

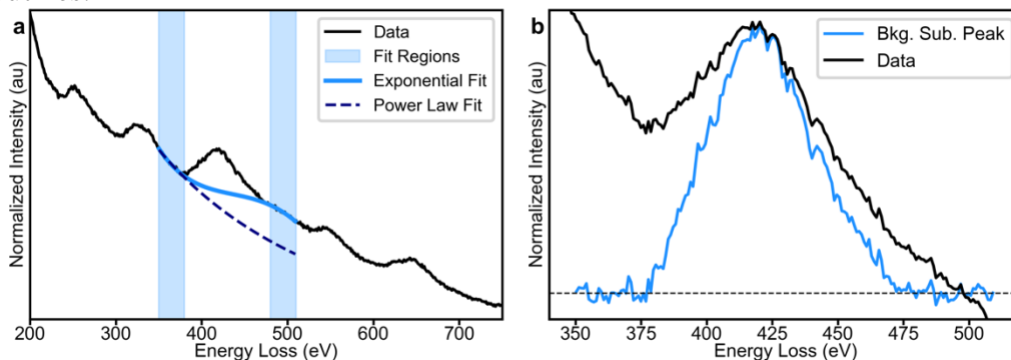
Supplementary Discussion 3: Data Processing of EEL Spectra

Figure 1 Spectrum Image Slices: In Figure 1, we compare 100 meV wide slices from two different spectrum-images to demonstrate the strength of the O-H vibrations in the filled tubes. For the filled CNT in Fig. 1 a 181 x 75 pixel spectrum-image was acquired with a 20 ms dwell time, for the empty tube a 151 x 78 pixel spectrum image was acquired with a 10 ms dwell time. In order to normalize, we use the maximum intensity of the ZLP in the pixel furthest away from the CNT, and find that the empty tube dataset had a total current a factor of 3.12 times less than the filled tube current. For the ‘counts’ reported in Main Text Fig. 1 for the empty tube we have multiplied the total counts in the empty tube slice by this factor of 3.12 to make it directly comparable to the filled tube slice, the filled tube slice intensity is as acquired. The spectra are not background subtracted to make sure the difficulties described in the following section do not influence the slices.

Additionally, due to our desire to minimize total beam-exposure on the CNTs between exposure, final preparations for the EELS acquisitions are done on a region of the sample a micron or two away from the CNT, then the stage is moved to get the CNT in range. As a result, a significant amount of drift is present in the spectrum-images. We assume the drift to be isotropic, fit the CNT positions as a function of the SI and then correct it using a linear fit. As a result, we have to cut out the areas of the dataset that are not aligned well between the top and bottom, and also cut out areas influenced by the SiN grid. The slices shown in the main text a fractional 120 x 36 pixel aligned region for both datasets.

The point spectra in Fig. 1d had energy resolutions of 8.5 meV for both CNTs, and for the bulk liquid cell. The spectrum images had energy resolutions of 9.5 meV for the filled CNT dataset, and 8.5 for the empty CNT dataset.

Background Subtraction for Spectra: All excitations in EELS are convolved with a background signal. For low-loss the excitations are convolved with the tail of the ZLP, and for core-loss they are convolved with the bulk plasmon tail. As a result, background subtraction is commonly employed to isolate the signal from the background. In core-loss EELS this is conventionally done with a power law, however, it has been demonstrated that in the low-loss region the ZLP tail is often better fit with more complex functions^{6,7}. Here, due to the combination bands discussed in Supplementary Discussion 1, fitting is challenging as strong peaks are in the regions directly before and after the ideal fitting regime, necessitating the use of one of these advanced fitting routines.



Supplementary Figure S18. Background Subtraction in vEELS. (a) A vEEL spectrum with the fit regions for a two-region, third-order exponential fit, and the resulting background. (b) Comparison of the background subtracted data and the actual peak.

We use the two-region, third-order exponential fit described in Ref. ⁶, which possesses the form $I(E) = e^{ax^3+bx^2+cx+d}$. The fitting regions are taken to be in regions on the tail or after the peak

of the combination band on the low-energy side of the O-H stretch regime (400-460) and before the onset of the next combination band on the high-energy side of the regime. An example of the fitting for the spectrum shown in Fig. S16 is shown in Fig. S18.

Figure S18a shows how the background fitting actual works. It is important to note that this background is not physical, it can clearly be seen that the pre-peak fitting region overlaps the preceding combination band. Moreover, the background level before the O-H stretch peak is not consistent with the background intensity after the peak. An example of how consistent background intensity would look is shown by fitting a power law in the pre-peak fitting region. The ZLP tail in this region follows this general line shape (continuous exponential decrease), the s-shape of the exponential fit is not a phenomenon that can originate directly from the elastic scattering intensity. We use this background subtraction method as a means of isolating the O-H stretch peak, which despite the non-physical nature of the background applied, does an excellent job of capturing the line-shape and frequency of the peak, as can be seen in the comparison between the raw data and the background subtracted peak shown in Fig. S18b.

Supplementary References

1. Bertie, J. E. & Lan, Z. Infrared Intensities of Liquids XX: The Intensity of the OH Stretching Band of Liquid Water Revisited, and the Best Current Values of the Optical Constants of H₂O(l) at 25°C between 15,000 and 1 cm⁻¹. *Appl. Spectrosc.* **50**, 1047–1057 (1996).
2. Krivanek, O. L. *et al.* Probing Biological Materials by Vibrational Analysis in the Electron Microscope. *Microsc. Microanal.* **28**, 1196–1197 (2022).
3. Jokisaari, J. R. *et al.* Vibrational Spectroscopy of Water with High Spatial Resolution. *Adv. Mater.* **30**, 1802702 (2018).
4. Scatena, L. F., Brown, M. G. & Richmond, G. L. Water at Hydrophobic Surfaces: Weak Hydrogen Bonding and Strong Orientation Effects. *Science* **292**, 908–912 (2001).
5. Abellan, P., Gautron, E. & LaVerne, J. A. Radiolysis of Thin Water Ice in Electron Microscopy. *J. Phys. Chem. C* **127**, 15336–15345 (2023).
6. Hachtel, J. A., Lupini, A. R. & Idrobo, J. C. Exploring the capabilities of monochromated electron energy loss spectroscopy in the infrared regime. *Sci. Rep.* **8**, 5637 (2018).
7. Fung, K. L. Y. *et al.* Accurate EELS background subtraction – an adaptable method in MATLAB. *Ultramicroscopy* **217**, 113052 (2020).